

UCLA

UCLA Electronic Theses and Dissertations

Title

Frequency stabilization of 554 nm light and measurement of molecular iodine hyperfine components

Permalink

<https://escholarship.org/uc/item/6cm1q290>

Author

Adams, Joshua Ross

Publication Date

2022

Peer reviewed|Thesis/dissertation

UNIVERSITY OF CALIFORNIA

Los Angeles

Frequency stabilization of 554 nm light and measurement of molecular iodine hyperfine
components

A thesis submitted in partial satisfaction
of the requirements for the degree Master of Science
in Physics

by

Joshua Ross Adams

2022

© Copyright by
Joshua Ross Adams.
2022

ABSTRACT OF THE THESIS

Frequency stabilization of 554 nm light and measurement of molecular iodine hyperfine components

by

Joshua Ross Adams

Master of Science in Physics

University of California, Los Angeles, 2022

Professor Wesley C. Campbell, Chair

I demonstrate a technique for frequency stabilization and modulation transfer spectroscopy using a low-cost external cavity laser (ECL) system. The 1108 nm pump beam is jointly locked to a cavity using the Pound-Drever-Hall technique and to an iodine transition using modulation transfer spectroscopy, with frequency stabilized to < 2 MHz. Absolute frequency measurements of molecular iodine hyperfine transitions at the frequency-doubled 554 nm are reported within a frequency region range of 1.4 GHz. The precision of measurements of each hyperfine component are within ± 2 MHz. The results suggest this application is appropriate for short-term frequency stabilization and measurements of hyperfine transitions, but more work is needed to determine if the system is viable for more advanced applications and trapped ion experiments.

The thesis of Joshua Ross Adams is approved.

Dolores Bozovic

Stuart Brown

Wesley C. Campbell, Committee Chair

University of California, Los Angeles

2022

Thank you to all of the wonderful staff and faculty members who always seem to be there at a moment's notice to answer questions, address concerns, or just serve as a wonderful resource for all things "graduate student." To Stephanie and Frank from the deepest part of my heart - thank you.

To Daniel Aharoni, thank you for inviting me into your neurophysics lab toward the end of my first year and for pushing me to develop my skills as a scientist. All of the time spent learning about microcontrollers, circuit boards, robotics, and neuroscience was invaluable and will forever be appreciated.

One of my biggest influences for reporting to UCLA's graduate program was Wes Campbell, who has always been a voice of reason and inspiration for me during my time in the program. With his guidance and under his direction, I graciously accepted the opportunity to complete the MS project as part of his ongoing research of quantum information science. Thank you, Wes. Your time, advice, assistance, and friendship will always be cherished.

The work performed within the MS thesis is a contribution to an STTR (Small Business Technology Transfer) in an effort to utilize frequency conversion and phase modulation to lock an 1108 nm pump laser to an iodine reference. The purpose of this task is to improve the stability of an 1108 nm pump beam source by investigating frequency doubling of the 1108 nm beam to 554 nm, and using it to perform a Doppler-free lock to the iodine reference. The project described herein was supported by the Air Force Research Lab (AFRL) through contract number FA864921P0966 and the task was performed under the direction of Dr. Wes Campbell. The content provided is solely the responsibility of the author and does not necessarily represent views of the AFRL.

Contents

1	Outline	1
1.1	Theory of Saturated Absorption Spectroscopy	2
1.2	Introduction to Fundamental Concepts	6
1.2.1	Electro-Optic Modulator	6
1.2.2	Acousto-Optic Modulator	8
1.2.3	Optical Isolator	10
1.2.4	Photodetector	11
1.2.5	Vapor Reference Cell	12
1.2.6	Second Harmonic Generation	13
1.3	Methods	15
1.3.1	Frequency Modulation Spectroscopy	15
1.3.2	Modulation Transfer Spectroscopy	18
1.3.3	Fabry-Perot Interferometer	22
1.3.4	Pound Drever Hall Technique	27
2	Experimental Setup	32
2.1	Preparation	32
2.1.1	Innolume Gain Module	32
2.1.2	Cavity Design	36
2.1.3	AdvR Fiber Modules	40
2.1.4	IntraAction AOM	42
2.1.5	Optics	43
2.1.6	Iodine Vapor Cell	44
2.1.7	High-Speed Servo Controller	45
2.2	Application of PDH Technique	46
2.2.1	Setup	46

2.2.2	Observing Cavity Modes	48
2.2.3	Locking to an Error Signal	48
2.3	Locking to an Iodine Reference	52
2.3.1	Getting on Resonance	52
2.3.2	Observing Saturated Absorption	55
2.3.3	Locking to an Error Signal	59
3	Experimental Results	63
3.0.1	Experimental Iodine Spectrum	63
3.0.2	Frequency Stability	66
4	Looking Ahead	68
4.1	Hardware	68
4.2	Moving Forward	70
5	Bibliography	71
	References	71

List of Figures

1	Key components of the project, with those highlighted being constructed and presented herein. An 1108 nm source will be used in conjunction with harmonic generators and modulators to stabilize frequency, eventually to apply to trapped ion experiments. Arrows represent beam path direction, while electronics and servo-controlled feedback are presented in detail within subsequent sections.	1
2	A higher-intensity pump beam (moving left) and a lower-intensity probe beam (moving right) overlap in an atomic vapor cell.	4
3	A representation of the Lamb dip in the Doppler broadened spectrum at some resonance frequency ν_0	5
4	The appearance of a central dip between two transitions due to there being a crossover resonance.	6
5	Example of an electro-optic phase modulator.	8
6	Diagrams showing first order frequency shifting in an AOM. The Up-shift represents a positive frequency shift and the Down-shift shows a negative shift, both of equal magnitude.	9
7	Optical configuration of a polarization-sensitive optical isolator with a Faraday rotator (45°) in between two polarizers.	11
8	A simplified setup using a vapor reference cell for spectroscopic applications.	13
9	Second harmonic generation via second-order nonlinear susceptibility, where ν_0 represents the incident beam frequency.	14
10	A laser at some carrier frequency ω_c is modulated to create a sideband at $\omega_c + \omega_m$. The modulated beam then passes through a sample where it acquires amplitude modulation before reaching a photodetector. The phase of the resultant signal is proportional to the frequency detuning.	17
11	A very basic configuration for frequency modulation spectroscopy.	18

12	(a) A pump beam ($E_1(t)$) with a frequency modulation of $+\Delta\omega$ and an unmodulated counter-propagating probe beam ($E_2(t)$) incident on a vapor cell (b) As a result of phase conjugation and four-wave-mixing within the nonlinear medium, a counter-propagating sideband accompanies the probe beam.	20
13	Left (forward phase conjugation): The wave passes through a conjugator, emerging as a phase conjugated wave, in which the point B, which formerly led point A in phase, now lags behind it by a corresponding amount. Right (backward phase conjugation): The conjugate wave travels in a direction opposite to that of the incident wave, traveling back upon itself.	20
14	Similar to the configuration for FMS, the higher-intensity pump beam is modulated for MTS.	22
15	Structure of a semiconfocal resonator with a concave mirror having a nonzero radius of curvature and a plane mirror.	23
16	Path length difference between two neighboring transmitted beams in a Fabry-Perot interferometer.	24
17	Some examples of transverse electromagnetic modes observed for a Fabry-Perot cavity.	26
18	Layout for Pound-Drever-Hall laser stabilization. The beam of a tunable laser is passed through a modulator and then reflected off a Fabry-Perot cavity before being received by a photodetector. The signal from the photodetector is then mixed down with a local oscillator before a low-pass filter, which isolates the signal needed for an error signal.	28
19	The form of Pound-Drever-Hall error signal when the modulation frequency is relatively-low.	31
20	External cavity scheme used for device characterization, showing how the gain-chip is oriented within the module and grating positioning.	33

21	Rendering of the gain module and grating mount platforms for the external cavity gain chip laser system.	34
22	Initial testing and current sweeps for the gain module output showing a linear relationship.	35
23	The initial PDH error signal showing a severe jitter and unstable signal, where the signal has a voltage division of 10.0 mV. The width of the graphic is ~ 6 MHz and the yellow line is a sweep signal of 140 kHz.	36
24	Diagram for the Fabry-Perot cavity used as part of the application of the PDH technique for frequency stabilization. Measurements are in inches.	37
25	With an equation for magnification, one can determine the total distance to focus to when aligning a scanning Fabry-Perot cavity.	39
26	The basic optical setup for the Fabry-Perot interferometer was completed using the focal distance determined by the equations for magnification. . . .	39
27	AdvR-designed SHG module used for second harmonic generation of a 554 nm beam incident upon the system discussed herein. Image provided courtesy of AdvR, 2021.	41
28	AdvR EOM used for frequency modulation of the incident beam upon the PDH lock. Image provided courtesy of AdvR, 2021.	42
29	Shown is the initial optical setup for the iodine component of the system and where modulation transfer spectroscopy occurs. This served to be an excellent starting point for initial testing, however a redesign of the optics to increase beam intensity and pump-probe overlap would be necessary.	44
30	The basic optical setup for locking to a cavity via the PDH technique.	46
31	The PDH lock and fundamental electronics are shown, with the servo controller feeding back directly into the diode controller for coarse current sweeps in this case.	47

32	An example of a clean error signal obtained while locking frequency to the Fabry-Perot cavity using the PDH technique.	49
33	Screen capture from the video camera used on the output of the Fabry-Perot cavity while locking to the TEM ₀₀ mode.	50
34	Initial demonstration of the working PDH lock in comparison to an unlocked gain module output, showing successful frequency stability. The red line represents frequency when the PDH lock is active while the black plot is the 1108 nm beam with no lock applied. The spike near the end of the locked signal was due to the laboratory doors being opened and shut, to be addressed in a subsequent section.	51
35	Frequency stabilization with an active PDH lock showing a maximum deviation of < 6 MHz during an interval over 40 minutes.	51
36	Observed fluorescence inside the iodine vapor cell during frequency sweeps. The shifted green absorption to yellow emission is characteristic of a Stokes Shift of ~ 25 nm.	52
37	The Stokes shift is the difference between the spectral position of the maximum of the first absorption band and the maximum of the fluorescence emission.	53
38	Region of the Doppler-broadened spectrum for iodine examined while performing current-driven frequency sweeps to obtain evidence of fluorescence at various locations. The box shows an area of initial recording of relatively-intense fluorescence. The black trace is the Doppler-broadened spectrum recorded by Salami and Ross [14].	54
39	A magnification of the previously-boxed localized region of initial recording of fluorescence on the Doppler-broadened spectrum for iodine. The black trace is the Doppler-broadened spectrum recorded by Salami and Ross [14].	55

40	Diagram for the revised optical setup for the iodine lock. Key changes made included the removal of a polarizing beam splitter at the very beginning of beam propagation and the addition of lenses to drastically reduce the beam waist while increasing beam overlap within the iodine vapor cell.	56
41	Power outputs and losses were measured at key sections within the optical setup to gain a better understanding of the system's efficiency and overall design. P_0 is the power of the 554 nm beam incident on the system, where each labeled loss represents a power loss with respect to the incident power. .	57
42	Top left: Only probe beam entering the vapor cell. Bottom left: Both probe and pump beam overlapping within the vapor cell. Right: Overlap of both graphics from the left, with evidence for saturated absorption represented as the green line. For this specific transition, each bump within the cluster was determined to be spaced by ~ 60 MHz. Here, the oscilloscope has a voltage division of 2.00 mV.	58
43	Fluorescence occurring within the iodine reference cell, as presented prior, however with a beam diameter of $< 400 \mu\text{m}$	59
44	Electronics setup for the iodine lock. Here driving the AOM for frequency modulation is a VCO and dithering oscillator routed through a bias tee into multiple signal amplifiers to adequately drive the modulator. The same oscillator is mixed with an amplified photodetector signal and sent through a low-pass filter of 16 kHz and servo controller feeding back into the Fabry-Perot cavity piezo in this case. Initially during locking to an iodine transition, the PDH lock was bypassed and the iodine lock servo controller feedback was sent directly to the laser diode controller.	60

45	Error signals with a near-zero background using modulation transfer spectroscopy, representing locations of hyperfine structures for iodine during frequency sweeping with the servo controller. This is a snapshot showing closely-spaced clusters, characteristic of error signals of hyperfine structures.	61
46	A visual representation of the presence of both a beam at some carrier frequency ν_0 and one with a modulation of $-\delta\nu$, with the zero-crossing at $\nu_0 - \frac{\delta\nu}{2}$	62
47	Confirmation of an examined region of the Doppler-broadened spectrum of iodine, where red regions of the spectrum represent those specifically mapped within an accuracy of ± 10 MHz. The black trace is the Doppler-broadened spectrum recorded by Salami and Ross [14].	63
48	A region of the iodine spectrum (transmission (%) vs wavenumber (cm^{-1})) examined during initial frequency sweeps and locking to a respective iodine transition. Green dots represent initial findings for lockable error signals representing locations of hyperfine components. The red dotted box represents the mentioned region of interest. The black trace is the Doppler-broadened spectrum recorded by Salami and Ross [14].	64
49	Error signal locations for hyperfine structures near 540.859237 THz. The black trace is the Doppler-broadened spectrum recorded by Salami and Ross [14].	66
50	Initial frequency stability while locked to an error signal at 540.859082 THz for ~ 40 minutes. The large fluctuation around 1500 seconds was due to ambient noise.	67

List of Tables

1	Some examples of relative widths of spectral features and broadening effects, with these values applicable to a region of $^{127}\text{I}_2$	2
2	Frequency measurements of the molecular iodine R(146) 25-0 $a_1 - a_9$ hyperfine components found at 554 nm, where R(146) represents the rotational branch (P,R) and J assignment and 25-0 is the vibrational assignment [27]. Measured Frequency values were recorded on the wave meter and Absolute Frequency values take into account the AOM modulated-frequency shift. Error on the frequency values is ± 2 MHz due to the absolute accuracy of the wave meter [20].	65

1 Outline

The overall goal of the encompassing project is to develop a fully integrated, compact, robust laser operating in the 369 nm spectral range for cooling, re-pumping, state preparation, and state detection of ytterbium-based Multi-Qubit Trapped Ion Systems (MQTIS). This will be completed by frequency conversion with phase modulation in a single integrated waveguide to produce > 10 mW of 369 nm light. To reach that step, testing of frequency conversion or harmonic generation of an 1108 nm beam source and frequency stabilization of that source is necessary to build upon. By applying concepts and methods of absorption spectroscopy in conjunction with applied optics, a successful system was realized and key progress was made.

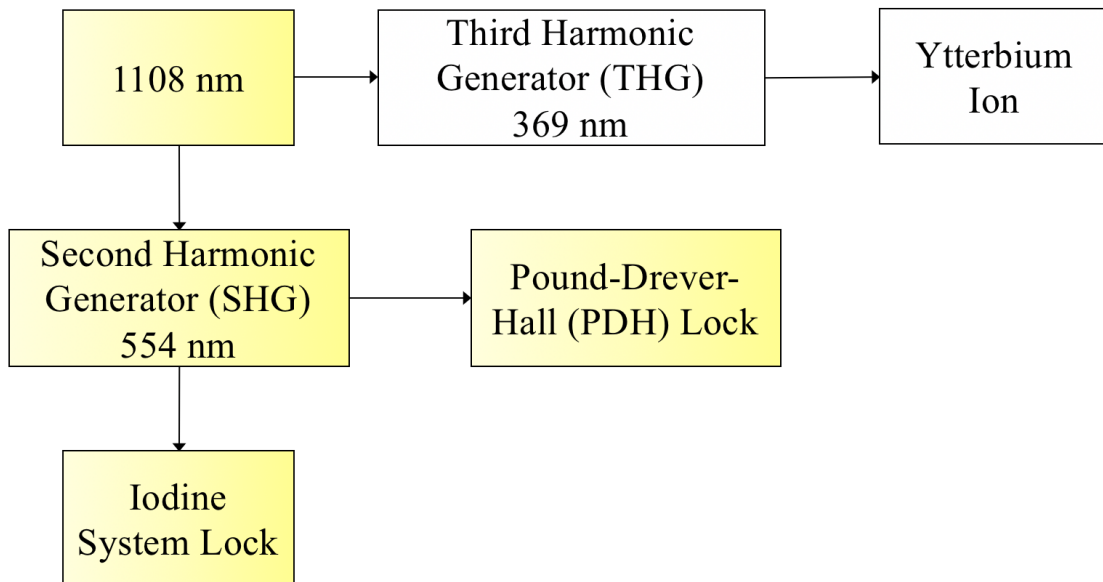


Figure 1: Key components of the project, with those highlighted being constructed and presented herein. An 1108 nm source will be used in conjunction with harmonic generators and modulators to stabilize frequency, eventually to apply to trapped ion experiments. Arrows represent beam path direction, while electronics and servo-controlled feedback are presented in detail within subsequent sections.

1.1 Theory of Saturated Absorption Spectroscopy

Absorption spectroscopy is based on the principle that electrons lie in quantized energy states, which allows an experimenter to obtain information about energy levels by the wavelengths of light that is absorbed. Measuring the power of the transmitted light as a function of the laser frequency, one can identify the frequencies of strong absorption.

There is a limit on spectral resolution due to various local effects which broaden a spectral linewidth or shape. Natural broadening is a result of energy states spontaneously decaying. This is an example of Heisenberg's Uncertainty Principal, as there is an uncertainty in the energy of a system due to an uncertainty in the lifetime of the state. A transition between two states will also not absorb or emit light at a single frequency but within a range of frequencies that can excite or de-excite a state, which leads to a naturally-broadened linewidth. Pressure broadening occurs due to the interaction between atoms or molecules as the perturbations may interrupt or cause a shift in the emission process. The duration of time for this process for an atom or molecule can change and this variation is ultimately proportional to the uncertainty associated with natural broadening. Power broadening can occur due to saturation, reducing the absorption near resonance while far from resonance the absorption changes little [26]. The limiting effect on resolution for this project is set by Doppler broadening, which is broadening of the atomic spectrum due to motion of atoms or molecules, and it is much larger than the previously mentioned broadening effects.

Spectral Dependence	Δ Frequency (MHz)
Doppler Broadening	$\sim 1.5 \times 10^3$
Hyperfine Structure	$\sim 3.0 \times 10^2$
Power Broadening	~ 5
Natural Broadening	$\sim 4 \times 10^{-1}$
Pressure Broadening	$\sim 1 \times 10^{-2}$

Table 1: Some examples of relative widths of spectral features and broadening effects, with these values applicable to a region of $^{127}\text{I}_2$.

From the reference frame of the atoms or molecules moving toward the laser beam, they will observe a Doppler blueshift in the frequency of light while atoms moving away observe a redshift in the frequency, which can be described by the Doppler-shift derived equation:

$$\delta\nu = \nu_l \frac{\delta v}{c}, \quad (1)$$

where $\delta\nu$ is the change in frequency between the frequency observed and the laser frequency in the lab frame, ν_l . δv is the velocity of the atom or molecule relative to the laser beam. Due to the distribution of velocities for any atomic or molecular gas, there will be a distribution of frequencies that can be absorbed for an atomic transition. At a thermal equilibrium, we can assume the velocities will follow a 3D Maxwellian distribution [24], which in only the x-direction can be represented as

$$n(v_x)dv_x = \left(\frac{m}{2\pi k_B T}\right)^{\frac{1}{2}} e^{-\frac{mv_x^2}{2\pi k_B T}} dv_x, \quad (2)$$

where k_B is the Boltzmann constant, m is the atomic mass, and T is temperature. Integrating over solid angle, a probability distribution of velocities can be obtained as

$$n(v)dv = 4\pi v^2 \left(\frac{m}{2\pi k_B T}\right)^{\frac{3}{2}} e^{-\frac{mv^2}{2\pi k_B T}} dv, \quad (3)$$

which gives the probability distribution of finding an atom or molecule with a speed near v . With the general formula for the Doppler effect, we can use velocity as a function of frequency to derive the Doppler-broadened frequency distribution to be

$$\Delta\nu_D = \nu_l \sqrt{\frac{8k_B T \ln(2)}{mc^2}}. \quad (4)$$

Letting $\sigma = \nu_l \sqrt{\frac{k_B T \ln(2)}{mc^2}}$, the frequency distribution becomes

$$\Delta\nu_D = 2\sqrt{2\ln(2)}\sigma, \quad (5)$$

which is an equation for the full width at half maximum (FWHM) of the broadened distribution. Using the technique of saturated absorption spectroscopy, Doppler broadening and this limitation on resolution can be overcome by singling out stationary atoms [24].

Before any beams pass through an atomic vapor, it can be assumed that nearly all of the atoms are in the ground state. When sending a low intensity or relatively weak "probe" beam through the vapor cell at a resonance frequency of a transition, normal absorption will occur and follow a Gaussian distribution. Now if a "pump" beam of higher intensity passes through the atomic vapor at the resonance frequency, there will be absorption that populates an excited state and depletes the ground state. When passing the probe beam through this depleted vapor, there will be fewer atoms to be excited than without the pump beam. This is what is meant by "saturated" in saturated absorption. The pump has saturated the transition.

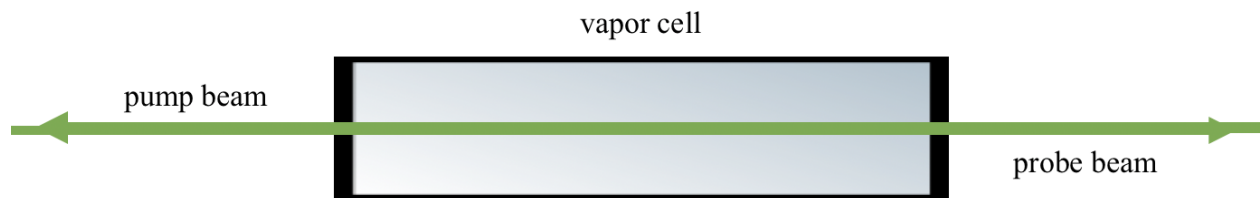


Figure 2: A higher-intensity pump beam (moving left) and a lower-intensity probe beam (moving right) overlap in an atomic vapor cell.

If we set up the system with a counter-propagating pump-probe scheme and consider that stationary atoms in the vapor cell absorb light at some frequency ν_0 , then for a beam with a frequency $< \nu_0$ there would need to be some upshift for an atom to interact with each respective beam. Whether the pump or probe beam, an atom would have to be moving toward the respective incoming beam. The same reasoning can be applied to a beam with a frequency $> \nu_0$. In this case, the atom would have to be traveling away from each respective incoming beam for an interaction to occur. With this in mind, it can be understood that

the two counter-propagating pump and probe beams can only interact with atoms traveling in opposite directions, relative to each beam. Therefore the beams will only jointly interact with atoms at frequency ν_0 , yielding a saturated ν_0 transition in turn reducing the absorption of the probe beam. The change or "dip" in the absorption spectrum of the probe beam for stationary atoms can be observed in the form of a Lamb dip [25]. The width of the dip is determined by a natural linewidth, collisions of the atoms within the vapor cell, and the spectral width of the beam (laser linewidth).

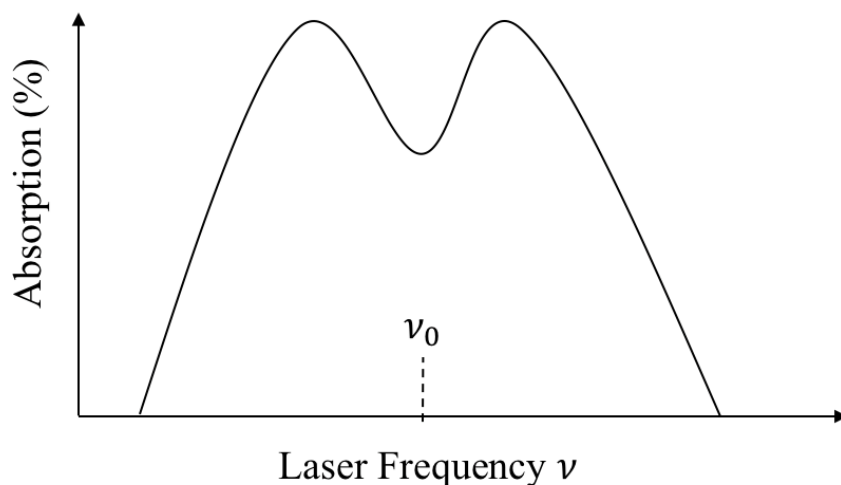


Figure 3: A representation of the Lamb dip in the Doppler broadened spectrum at some resonance frequency ν_0 .

The technique of saturated absorption spectroscopy allows one to measure sharp Doppler-free features within a Doppler-broadened spectrum for a given atomic vapor sample.

It should be noted that when pairs of transitions have energy levels in common and a separation less than the Doppler width, additional peaks or crossover resonances will appear exactly between the transitions at the frequency

$$\frac{(\nu_1 + \nu_2)}{2}, \quad (6)$$

with the transitions being at frequency ν_1 and ν_2 , respectively. While this property does convolute observation of saturated absorption, due to the midway symmetry, identifying crossover resonances and surrounding transition peaks is generally not difficult [26].

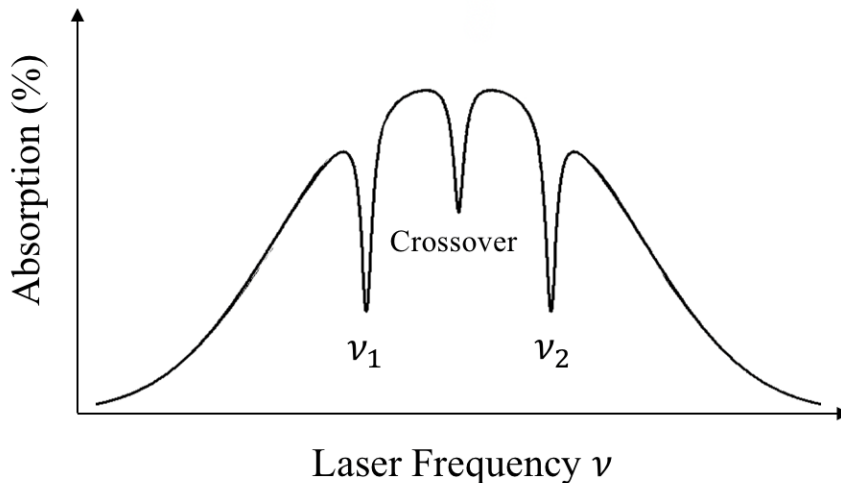


Figure 4: The appearance of a central dip between two transitions due to there being a crossover resonance.

1.2 Introduction to Fundamental Concepts

1.2.1 Electro-Optic Modulator

To understand how an electro-optic modulator (EOM) works, it is beneficial to review the Pockels effect, which is a specific example of an electro-optic effect. The Pockels effect rotates the polarization of incident light as a function of the externally applied electrical field and is a property of certain crystals. This can be acquired longitudinally or transversally with respect to the wave vector of the light beam. In both cases the anisotropic refractive index will couple the two electric fields such that light polarization becomes a function of optical path in a crystal [2]. Thus the incident linearly polarized light is converted to circular polarization, to linear polarization rotated by 90° , to circular polarization, to linear polarization rotated by 180° and so on. For a certain external electric field, the crystal works as a quarter wave plate, producing circular polarized light, and for twice this field as a half wave plate, producing

linear but 180° rotated light. The change of the refractive index of the matter is in the first approximation a linear function of the external electric field. Thus, this type of second-order nonlinear electro-optical effect is sometimes called linear although the interaction with the light finally shows a quadratic dependence on the total electric field [2].

An EOM is a signal controlled optical device that works via the electro-optic effect and serves to modulate phase, frequency, amplitude, or polarization of a light beam. For some crystals, refractive indices are functions of the electrical field applied to them, where the changing index is linearly proportional to the applied field magnitude. Figure 5 shows an example of an electro-optic phase modulator made with a popular optical waveguide material, LiNbO_3 , and a pair of electrodes. If the length of the electrode is L , the separation between the two electrodes is d , and the applied voltage is V , the optical phase change introduced by the linear electro-optic effect is

$$\phi(V) = \left(\frac{2\pi\alpha_{\text{EO}}L}{\lambda d} \right) V, \quad (7)$$

where α_{EO} represents the linear electro-optic coefficient and λ the wavelength of light. The modulation efficiency, defined as $\frac{d\phi}{dV}$, is directly proportional to the length of the electrode L and inversely proportional to the electrode separation d . Therefore increasing length and reducing separation would increase modulation efficiency but lead to an increase in parasitic capacitance, reducing modulation speed [9].

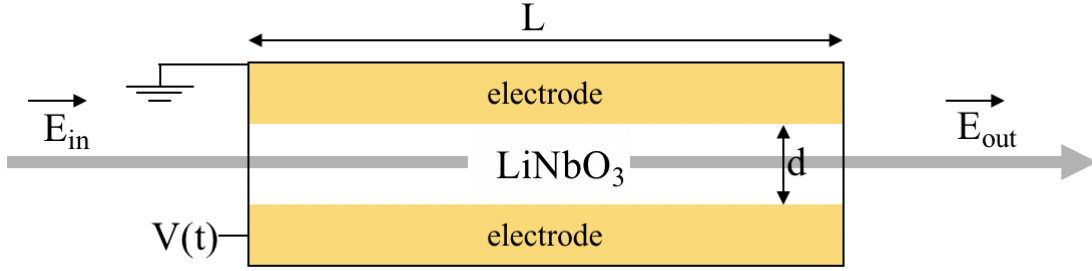


Figure 5: Example of an electro-optic phase modulator.

1.2.2 Acousto-Optic Modulator

An acousto-optic modulator (AOM) deflects a beam of light at an index grating which is induced by hyper-sound waves in crystals. The sound wave is typically supplied by a piezo-driver in the MHz range [2]. As the beam and AOM are operated continuously, the output consists of a periodical series of output pulses. The frequency of the AOM manifests as sidebands accompanying the original carrier in the beam. Another way to put this is as follows: When an RF frequency acoustic wave propagates inside an optically transparent medium, a period change in refractive index occurs due to the compressions and rarefactions of the sound wave. This periodic variation produces a grating capable of diffracting an incident laser beam [3].

There are three common modes of operations for an AOM: deflection, modulation, and frequency shifting. By turning on and off the acoustic power source or varying the frequency, the AOM can serve as a rapid light deflector. This property of allowing a beam to be moved rapidly in space without any necessary moving parts has been applied to laser printers and laser display devices. Modulation of the intensity of the diffracted light beam can occur by simply modulating the power of the acoustic wave source. This is because the amount of light diffracted to the first order beam is dependent upon the amplitude of the acoustic waves that diffract the incident beam. This mechanism can be used to modulate a beam as

part of an optical communications system containing various forms of digital media [2].

Frequency shifting is one of the most useful properties of an AOM and is of particular interest to our application. As the acoustic wave travels across the beam, the optical frequency experiences a Doppler shift by an amount that is equal to the acoustic frequency which is modulated up or down depending on the orientation of the optical beam relative to the sound field. If the laser beam enters at a Bragg angle in opposition to the field, an up-shift occurs (plus first order), where the optical frequency experiences in a down-shift if the beam enters at a Bragg angle in the same direction as the field (minus first order) [3]. This is shown in Figure 6.

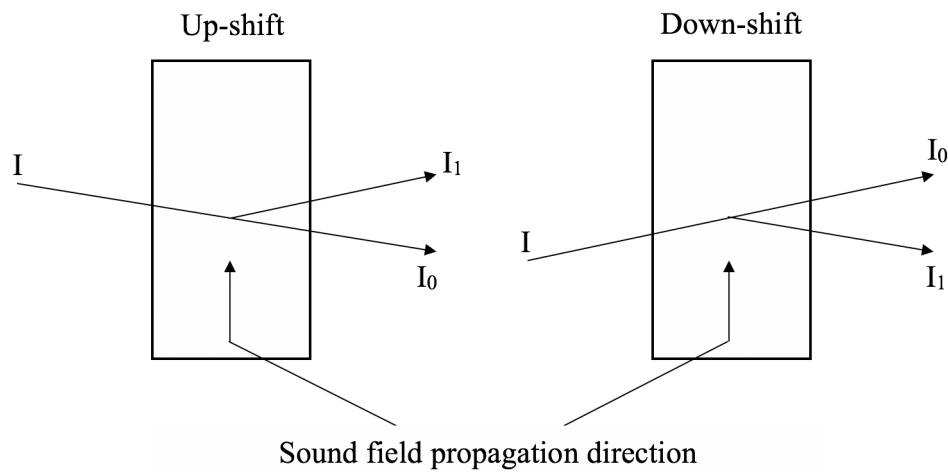


Figure 6: Diagrams showing first order frequency shifting in an AOM. The Up-shift represents a positive frequency shift and the Down-shift shows a negative shift, both of equal magnitude.

Light diffracted by an acoustic wave of a single frequency can produce two types of diffraction, however we are interested in Bragg diffraction, which occurs when $L > \frac{\Lambda^2}{\lambda}$, where L is the light-sound interaction length, Λ is the sound wavelength, and λ is the laser wavelength. In

this mode, the incident laser beam should enter the sound field at the Bragg angle [3]

$$\theta_B = \frac{\lambda}{2\Lambda}. \quad (8)$$

Maximum diffraction efficiency occurs when the incident beam and first order diffracted beam are adjusted to form symmetrical angles with respect to the acoustic wavefronts. Since AOM devices are not 100% efficient, all of the light cannot be removed from the zeroth order; however, no light remains in the first order when the power is removed. This property has led to the first diffracted order being used in acousto-optic devices.

1.2.3 Optical Isolator

An optical isolator is a device that allows an optical signal to travel in one direction while preventing reflections from traveling in the reverse direction. They are incorporated as a fundamental component in many optical systems and applications as they serve to reduce hurdles of optical systems such as phase noise, intensity noise, and overall wavelength instability. Thus, an optical isolator is usually required at the output of each laser diode in applications that require low optical noise and stable single optical frequency. Another example is in an optical amplifier where unidirectional optical amplification is required. In this case, the bidirectional nature of optical amplification of the optical gain medium would cause self-oscillation if the external optical reflection from connectors and other optical components is strong enough [6].

A traditional optical isolator is based on a Faraday rotator in between two polarizers, as shown in Figure 7. In this configuration, the optical signal coming from the left side passes through the first polarizer whose optical axis is in the vertical direction, which matches the polarization orientation of the input optical signal. Then, a Faraday rotator rotates the polarization of the optical signal by 45° in a clockwise direction. The optical axis of the

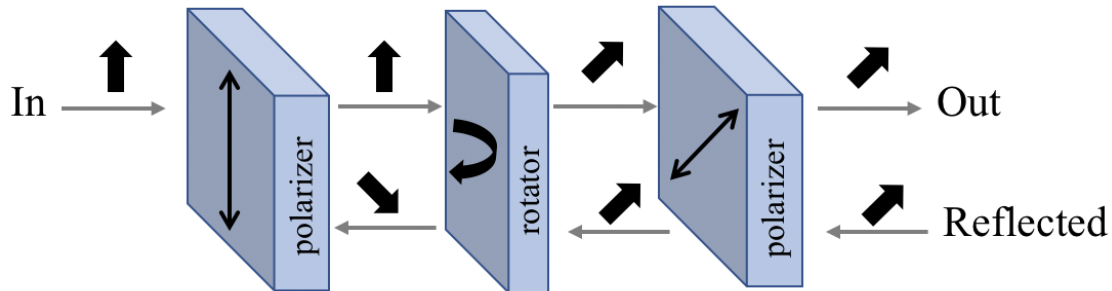


Figure 7: Optical configuration of a polarization-sensitive optical isolator with a Faraday rotator (45°) in between two polarizers.

second polarizer is oriented 45° with respect to the first polarizer, which allows the optical signal to pass through with little attenuation. If there is a reflection from the optical circuit at the right side, the reflected optical signal has to pass through the Faraday rotator from right to left. Since the Faraday rotator is a nonreciprocal device, the polarization state of the reflected optical signal will rotate for an additional 45° in the same direction as the input signal, thus becoming horizontal, which is perpendicular to the optical axis of the first polarizer. In this way, the first polarizer effectively blocks the reflected optical signal and assures the unidirectional transmission of the optical isolator [6].

1.2.4 Photodetector

To obtain a useful incoming optical signal, it must be converted into an electrical signal using a photodetector. The most commonly used form of these kinds of devices are semiconductor photodetectors, also known as photodiodes, due to their small size, fast detection speed, and high efficiency. Similar to the structures of laser diodes, photodiodes are based on the PN junctions; however, the PN junction of a photodetector is biased so that only a very small reverse saturation current flows through the diode without an input optical signal. Although the basic structure of a photodiode can be a simple PN junction, practical photodiodes can have various device structures to enhance quantum efficiency. For example, the popular PIN structure has an intrinsic layer sandwiched between the p- and n-type layers, and that is

why a semiconductor photodetector is also known as a PIN diode [7].

In an ideal situation, each photon received is translated into a free electron so that a photocurrent is linearly proportional to the power of the incoming optical signal. This unfortunately is not the case for a practical semiconductor material [7]. The overall response and efficiency of a photodiode depends on a number of factors which include bandgap structures, material quality, photonic structure, electrode design, and noise (shot, thermal, and dark-current) generated during the photodetection process. Shot noise is intrinsically associated with photodetection and sets the fundamental limit of the optical system's performance known as the quantum limit [7]. Thermal noise and dark-current noise, however, can be reduced with efforts. For example, by increasing the load resistance, thermal noise can be diminished and by decreasing the reverse saturation current, dark-current noise may be reduced.

Since photocurrent is proportional to the received signal optical power, which is the square of the signal optical field, a photodiode is also known as a square-law detector. This squaring process can generate mixing products between different frequency components of the received optical field, as well as the mixing between optical signal and the broadband optical noise which introduces beats in the electric domain [7]. These beats plays an instrumental role in receiving and interpreting signals pertaining to laser frequency locking and spectroscopy.

1.2.5 Vapor Reference Cell

A reference cell contains a specific atomic or molecular vapor, which has a well-defined absorption spectrum to be used in spectroscopic applications such as laser calibration, laser stabilization, and wave meter calibration. Since each fill material is associated with a unique absorption spectrum that serves as its fingerprint, the content of a reference cell can be determined via a linear absorption measurement, as shown in Figure 8. By scanning a

tunable laser over a wavelength range and detecting light absorption with a photodetector, peaks that are characteristic of the vapor will be recorded [10].

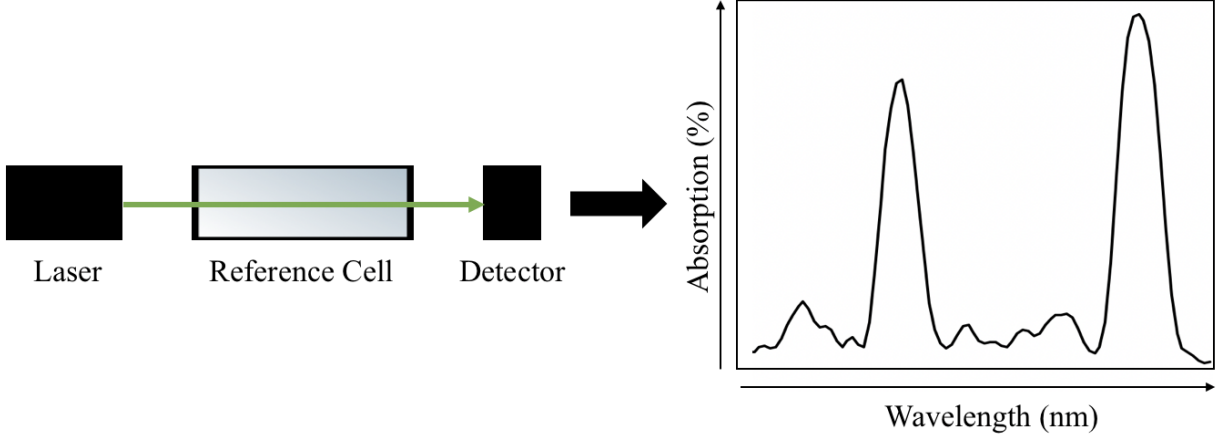


Figure 8: A simplified setup using a vapor reference cell for spectroscopic applications.

1.2.6 Second Harmonic Generation

In second-order nonlinear optics, two different light waves can superimpose and generate the following nonlinear polarization:

$$\mathbf{P}^{(2)} = \epsilon_0 \chi^{(2)} \mathbf{E}_1 \mathbf{E}_2. \quad (9)$$

If there are two equal monochromatic light waves with the same polarization, frequency ν_0 , and direction k_0 , the second-order nonlinear polarization is determined by the product of the two electric fields [2]. The second-order nonlinear polarization can then be represented as

$$\begin{aligned} \mathbf{P}^{(2)} &= \epsilon_0 \chi^{(2)} \mathbf{E}_1 \mathbf{E}_2 = \epsilon_0 \chi^{(2)} \mathbf{E}^2 \\ &= \epsilon_0 \chi^{(2)} \{E_0(\mathbf{k}, \phi) \cos(2\pi\nu_0 t)\}^2 \\ &= \frac{1}{2} \epsilon_0 \chi^{(2)} E_0^2(\mathbf{k}, \phi) + \frac{1}{2} \epsilon_0 \chi^{(2)} \mathbf{E}_0^2(\mathbf{k}, \phi) \cos(4\pi\nu_0 t) \\ &= \mathbf{P}^{(2)}(\nu_0) + \mathbf{P}^{(2)}(2\nu_0). \end{aligned} \quad (10)$$

This polarization shows a second term that oscillates with twice the frequency of the incident wave, thus emitting a light wave with twice the frequency of the incident wave and producing the second harmonic via second harmonic generation (SHG) [2]. This second-order nonlinearity can be used to generate light of twice the photon energy, allowing blue light from red or green light from infrared.

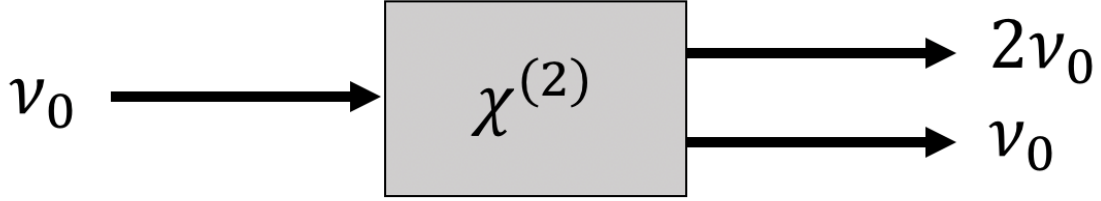


Figure 9: Second harmonic generation via second-order nonlinear susceptibility, where ν_0 represents the incident beam frequency.

Similarly, the generation of a third harmonic or generation of light three times the incident frequency can be achieved via the third-order nonlinearity. Although even after reducing components of the third-order nonlinear polarization, a matrix with 30 different values remains [2]. However if the material used is isotropic, the third-order nonlinear polarization reduces to

$$P_m^{(3)} = \epsilon_0 e_{11} (E_m \mathbf{E} \mathbf{E}), \quad (11)$$

where $m = x, y, z$ and e_{11} represents the first matrix element of the tensor $\chi^{(3)}$. The three light fields can be components of the same light beam but can also be three different light beams which overlap in the nonlinear material. If a fourth beam is incorporated to detect changes in the nonlinear material, a mechanism called four wave mixing occurs; which will be further discussed in a subsequent section.

1.3 Methods

1.3.1 Frequency Modulation Spectroscopy

At any point in space, in its simplest form, the electric field of a traveling monochromatic electromagnetic wave can be described by

$$E_1(t) = E_0 \sin(\omega_c t), \quad (12)$$

where E_0 is the peak field amplitude and ω_c is the carrier frequency. If ω_c is phase modulated sinusoidally at some modulation frequency ω_m , then it can be treated as having a carrier ω_c with sidebands spaced at intervals of ω_m :

$$\begin{aligned} E_2(t) &= E_0 \sin[\omega_c t + \delta \sin(\omega_m t)] \\ &= E_0 \sum_{n=-\infty}^{\infty} J_n(\delta) \sin\{[\omega_c + n\omega_m]t\}, \end{aligned} \quad (13)$$

where δ is the modulation index, $J_n(\delta)$ are Bessel functions and $\delta = \frac{\omega_D}{\omega_m}$. ω_D represents the peak frequency deviation.

If $\omega_D < \omega_m$, then all sidebands other than $J_{\pm 1}$ may be neglected. This leads to

$$E_2(t) = E_0 \left\{ \frac{\delta}{2} \sin[(\omega_c + \omega_m)t] + \sin(\omega_c t) - \frac{\delta}{2} \sin[(\omega_c - \omega_m)t] \right\}, \quad (14)$$

which shows the initial carrier with an accompanied modulation manifested as sidebands of frequency ω_m .

Frequency modulated spectroscopy (FMS), also referred to as optical heterodyne spectroscopy, involves phase or frequency modulating a probe beam and measuring the differential absorption experienced by each frequency modulated sideband as it traverses a saturated medium. The

modulation of the probe beam can be performed with devices like an EOM or AOM outside of a laser cavity, which allows an experimenter to monitor both the unmodulated and modulated beams [2].

The fundamental property of FMS is the modulation of the laser frequency and its effect on the intensity of light transmitted by a vapor cell with some absorption line. The attenuation and the phase shift experienced by each frequency component unbalances the phase-modulated light, resulting in a time-varying intensity that is proportional to $|E(t)|^2$. With a square-law photodetector and phase-sensitive detection electronics such as a lock-in amplifier or mixer, a signal that is modulated can be coherently detected [5]. A signal is obtained from the beating of the frequency components that are separated by the modulation frequency ω_m .

In a situation where the frequency at which the laser is modulated is low and the amplitude of that modulation is small relative to the unmodulated beam, the laser carrier frequency can be thought of as periodically increasing and decreasing by a small amount. If the laser frequency is in the vicinity of an absorption line, then the frequency modulation causes the absorption to modulate synchronously. In this way, the laser frequency modulation is mapped onto the laser's transmitted intensity. Essentially, the frequency modulation on the laser has been transformed into an amplitude modulation by the absorption. This change allows a photodetector to register the modulation, since a photodetector does not directly detect frequency changes.

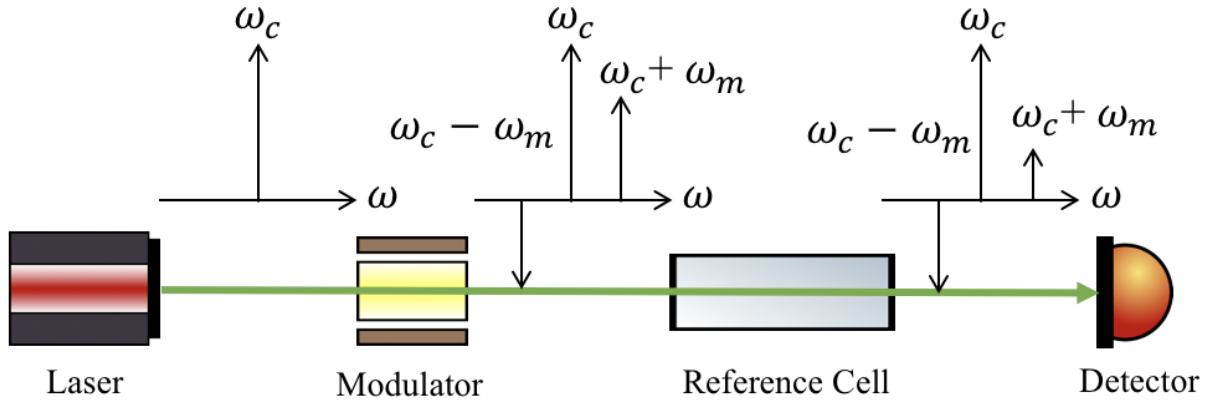


Figure 10: A laser at some carrier frequency ω_c is modulated to create a sideband at $\omega_c + \omega_m$. The modulated beam then passes through a sample where it acquires amplitude modulation before reaching a photodetector. The phase of the resultant signal is proportional to the frequency detuning.

The FMS condition is achieved when ω_m is large compared with the spectral feature of interest and only one sideband probes the spectral feature [11]. This sideband can be scanned through the spectral feature either by tuning the input laser frequency ω_c or by tuning the radio frequency (RF) ω_m . In either case, the losses and phase shifts experienced by the carrier and lower sideband remain essentially constant. The in-phase component of the beat signal is directly proportional to the absorption induced by the spectral feature, whereas the quadrature component is directly proportional to the dispersion induced by the spectral feature. The RF beat signal arises from a heterodyning of the modulated sidebands with the carrier frequency, and thus the signal strength is proportional to the geometrical mean of the intensity of each sideband and the carrier [11].

After the phase is adjusted for the optimal signal amplitude and slope, the result can be used directly as a dispersive error signal. To resolve sub-Doppler details using FMS, typically a counter-propagating unmodulated pump beam is sent through the sample to saturate it, analogous to saturated absorption spectroscopy without modulation. Now the modulated

probe beam detects sub-Doppler features in the spectrum, which have steep slopes and are ideal for locking. The signal obtained is dispersive, as in the single-beam case, and can be directly used as an error signal.

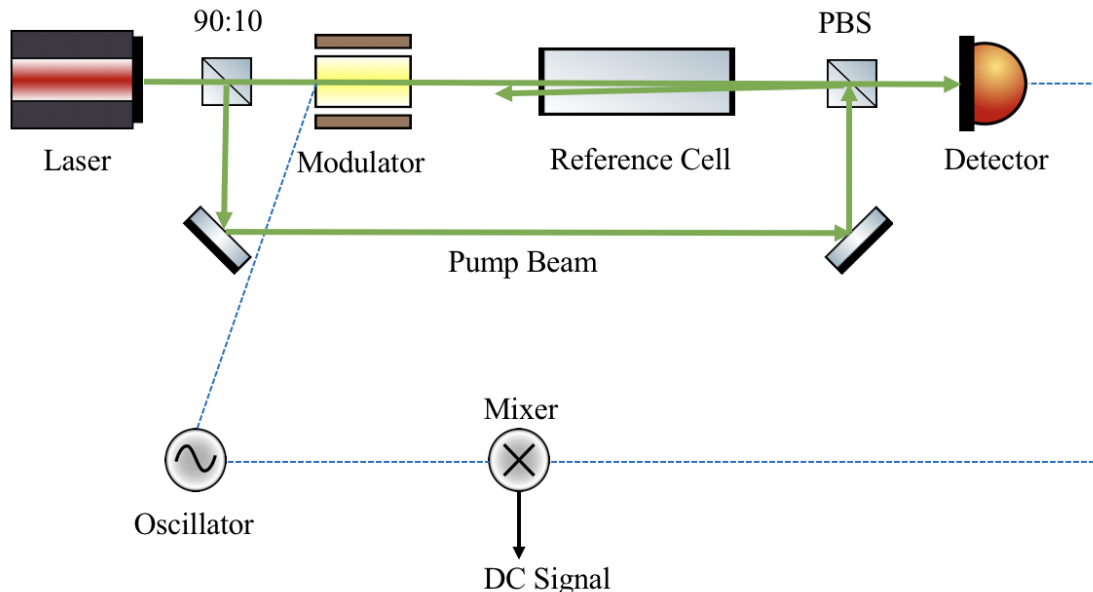


Figure 11: A very basic configuration for frequency modulation spectroscopy.

1.3.2 Modulation Transfer Spectroscopy

A method built upon FMS that is known to provide high-amplitude error signals with near zero background, allowing for increased stability for measurements of hyperfine components and frequency locking, is modulation transfer spectroscopy (MTS). This technique uses a nonlinear interaction of multiple wavelengths in the presence of a medium called four-wave-mixing which ultimately creates a phase conjugation [17] that yields additional propagating waves or sidebands which are transferred to a counter-propagating beam. Looking at a simplified example of a pump beam with a single sideband and a counter-propagating probe beam overlapping in a vapor cell, the electromagnetic waves may be written as

$$E_1(t) = \frac{1}{2} [E_1 e^{i(kz - \omega t)} + cc] \quad (\text{pump}) \quad (15)$$

$$E_2(t) = \frac{1}{2} [E_2 e^{-i(kz+\omega t)} + \text{cc}] \quad (\text{probe}) \quad (16)$$

$$E_3(t) = \frac{1}{2} [E_3 e^{i[kz-(\omega+\Delta\omega)t]} + \text{cc}] \quad (\text{sideband}) \quad (17)$$

where cc represents $[E_j e^{i(kz-\omega t)}]^*$ ($j = 1, 2, 3, \dots$) and

$$\omega_1 = \omega_2 = \omega$$

$$\omega_3 = \omega + \Delta\omega$$

where $\Delta\omega$ is small

$$k_1 = k_2 = k$$

$$k_3 = -k_1 = -k$$

Higher-order polarization terms are present with one representing the fourth wave generated as

$$P^4 \propto \epsilon_0 \chi^{(3)} E_1(t) E_2(t) E_3^*(t). \quad (18)$$

This leads to an additional wave in the direction of the counter-propagating probe beam,

$$E_4(t) = E_1 E_2 E_3^* e^{i[-kz-(\omega-\Delta\omega)t]} + \text{cc}, \quad (19)$$

where matching conditions are satisfied

$$k_1 + k_2 = k_3 + k_4$$

$$\omega_1 + \omega_2 = \omega_3 + \omega_4$$

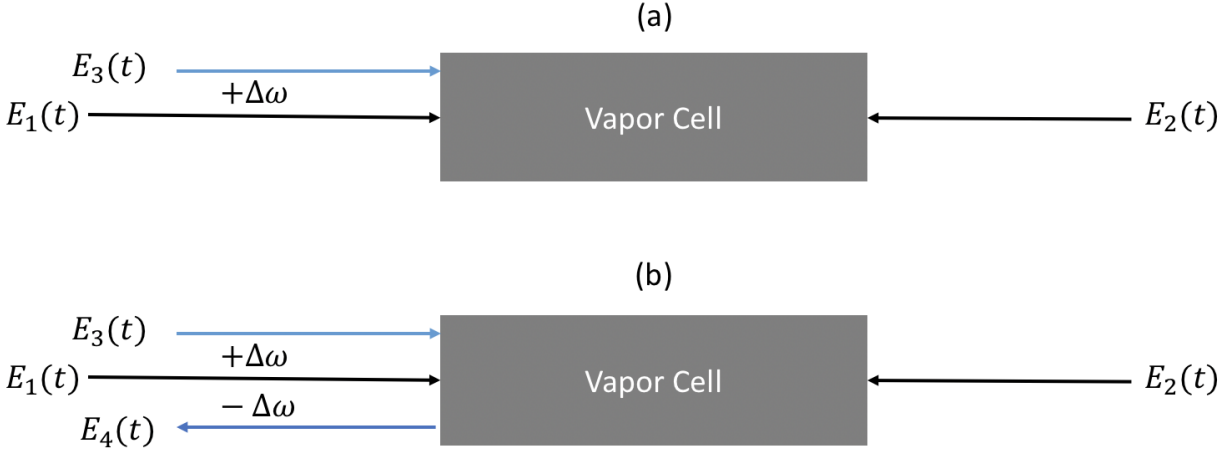


Figure 12: (a) A pump beam ($E_1(t)$) with a frequency modulation of $+\Delta\omega$ and an unmodulated counter-propagating probe beam ($E_2(t)$) incident on a vapor cell (b) As a result of phase conjugation and four-wave-mixing within the nonlinear medium, a counter-propagating sideband accompanies the probe beam.

This is a demonstration of four-wave-mixing within a nonlinear medium to create what can be interpreted to be a phase conjugation occurring within the nonlinear vapor. Figure 13 provides a visual representation of forward and backward wave propagation when interacting with a phase conjugator; in our case, a nonlinear medium in the form of a vapor cell.

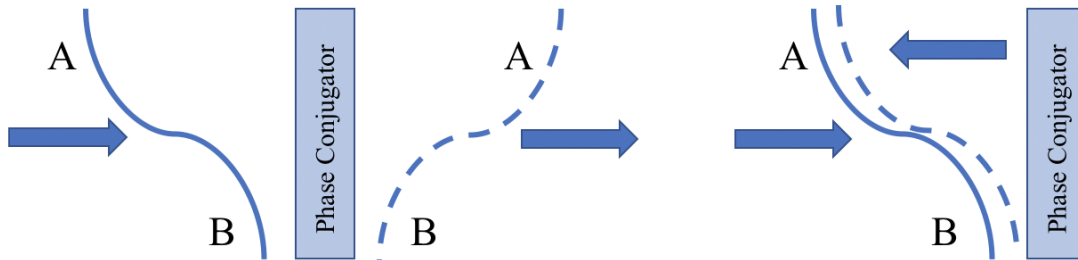


Figure 13: Left (forward phase conjugation): The wave passes through a conjugator, emerging as a phase conjugated wave, in which the point B, which formerly led point A in phase, now lags behind it by a corresponding amount. Right (backward phase conjugation): The conjugate wave travels in a direction opposite to that of the incident wave, traveling back upon itself.

A mechanism to discuss for modulation transfer is reflection [29], which is related to phase

conjugation. Saturation induces a partial standing-wave field pattern in the populations of the resonant states. The resulting spatial periodicity in the transparency of the medium acts as a diffraction grating to Bragg-reflect a portion of either laser beam back in the direction of the other [29]. This mechanism allows for a probe-beam sideband to produce a sideband for the counter-propagating saturating beam. A probe sideband will then interfere with the pump to induce a moving grating structure, and when the probe carrier reflects from the grating, it is Doppler shifted, also becoming a sideband of the saturating beam.

MTS was the method of choice for the experimental setup presented herein due to some key benefits related to error signal generation and stability. One characteristic of MTS is that steep, dispersive signals only exist for cycling transitions and signals are suppressed for transitions to states other than the ground state. This is due to the decay of the ground state population, where interaction time between atoms or molecules and a beam is proportional to a suppressed signal [28]. The lack of linear background absorption also provides a relatively low sensitivity to the environment, assisting with system and locking stability.

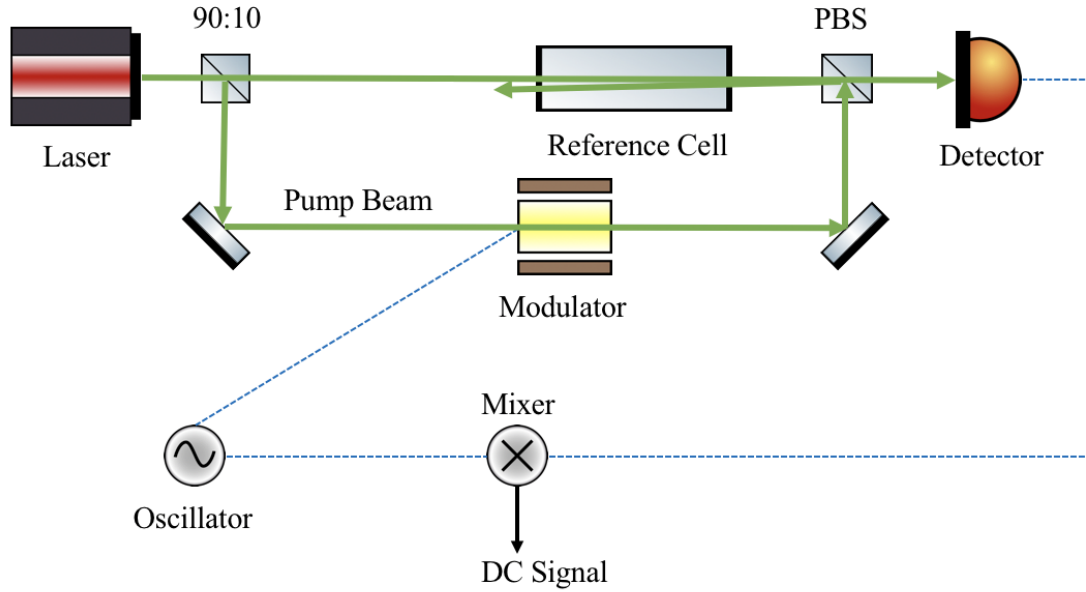


Figure 14: Similar to the configuration for FMS, the higher-intensity pump beam is modulated for MTS.

1.3.3 Fabry-Perot Interferometer

A laser resonator (or cavity) can be designed as a stable resonator to produce a standing light wave from the interference of two counter-propagating light beams with a certain transversal and longitudinal distribution of the electric field inside. These distributions are eigensolutions of Maxwell's equations for the standing light wave with the boundary conditions of the curved resonator mirror surfaces [2]. The transversal structures of these eigensolutions are called transversal resonator modes, where the transversal structure can change along the axis of the laser and a transversal light pattern will be observed behind the partially transparent resonator mirror or an output coupler. For many applications a Gaussian beam is required as the transversal mode of the laser. The curvatures of the wave fronts of the resonator modes of the light beam at the position of the mirror surfaces are the same as the curvature of the mirrors. This condition defines the possible transversal modes of a stable resonator.

The axial structures of these eigensolutions are the longitudinal resonator (or axial) modes [2]. The standing light wave is built by the interference of the back and forth moving light waves reflected at the mirrors. The electric field has a knot at the mirror surface and thus the longitudinal modes are selected. There are numerous stable empty resonator or cavity constructions, however we shall ignore all but the semiconfocal configuration; which is what the experiment presented herein utilizes. Semiconfocal resonators typically have the beam waist at one mirror which is planar.

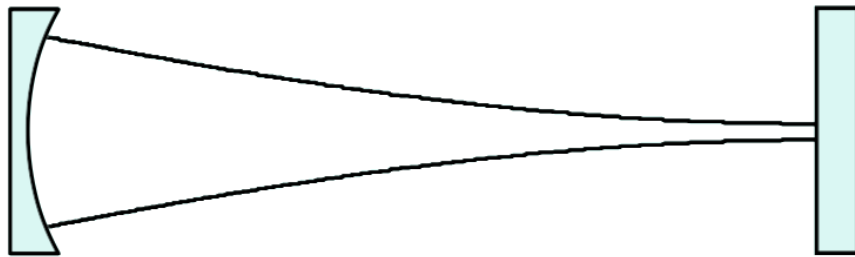


Figure 15: Structure of a semiconfocal resonator with a concave mirror having a nonzero radius of curvature and a plane mirror.

A Fabry-Perot interferometer (also known as a Fabry-Perot cavity or etalon) is an optical cavity with two parallel high-quality planar reflectors. At the mirror surfaces, the R_e th share of the electric light field will be reflected and the T_e th share will be transmitted. The index e indicates the reflectivity and transmission related with the electric field of the light. The reflectivity R and the transmission T related to the intensity will be: $R = R_e^2$ and $T = T_e^2$. The transmitted and reflected light waves will interfere with their phase relations as a function of the incident wavelength, the length L and the reflectivity of the interferometer. The path length difference between one transmitted beam and the next, which is twice more reflected, is equal to $\delta z = l_1 + l_2$, as shown in Figure 16.

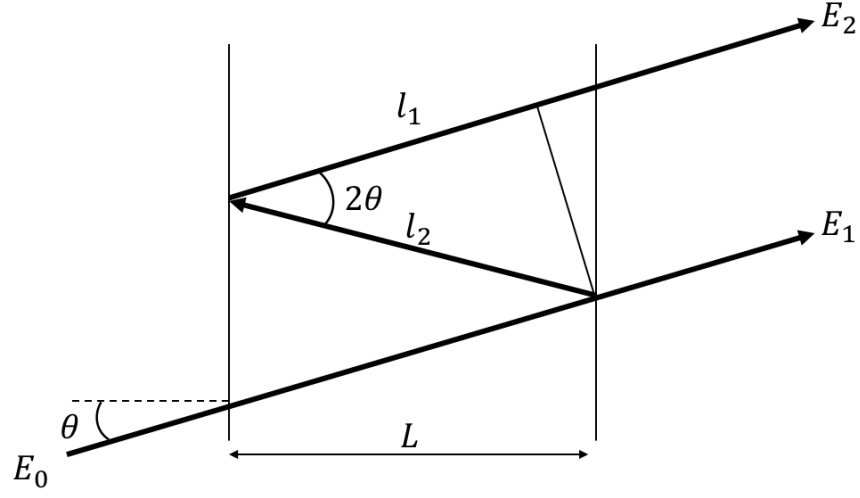


Figure 16: Path length difference between two neighboring transmitted beams in a Fabry-Perot interferometer.

This path length difference [2] δz follows from

$$\delta z = l_1 + l_2 = \frac{L}{\cos \theta} + \frac{L \cos 2\theta}{\cos \theta} = 2L \cos \theta, \quad (20)$$

resulting in a phase difference ϕ , being

$$\phi = |\mathbf{k}| \delta z = \frac{4\pi}{\lambda} L \cos \theta, \quad (21)$$

with light wavelength λ . The total transmitted field E_T is

$$E_T = E_0 T_e^2 \frac{1}{1 - R_e^2 e^{i\phi}} \quad (22)$$

and the total transmitted intensity is

$$I_T = I_0 \frac{T^2}{(1 - R_e e^{i\phi})^2}, \quad (23)$$

with transmission T and reflectivity R related to intensity, and I_0 as the intensity of the

incident light. The phase shift ϕ can also contain possible additional phase shifts from the reflection at the mirrors [2]. The formula can be written in real form as

$$I_T = I_0 \frac{T^2}{(1-R)^2} \frac{1}{1 + \frac{4R}{(1-R)^2} \sin^2\left(\frac{\phi}{2}\right)} = I_0 \frac{T^2}{(1-R)^2} f(\phi), \quad (24)$$

where $f(\phi)$ is the Airy function, which describes the total transmission of the Fabry-Perot interferometer with no absorption losses ($T + R = 1$).

It should be noted that even Fabry-Perot interferometers with very high reflectivity values ($R > 0.999$) can show 100% total transmission if the wavelength is tuned to the path length L and the spectral bandwidth is small enough. This result is a consequence of accumulated high intensity inside the interferometer, which demands sufficiently long coherence lengths and thus long pulse durations of the light used. For high power applications, the damage threshold of the mirror surfaces should be checked for increased internal intensity.

The m th transmission maximum occurs at $\phi_{\max} = 2m\pi$ and it follows the position of transmission maxima is

$$\frac{L}{\lambda} \cos \theta_m = \frac{m}{2} \quad (25)$$

and transmission minima is

$$T_{\min} = \frac{T^2}{(1+R)^2} \approx \frac{T^2}{4}, \quad (26)$$

with the approximation for large reflectivities ($R \approx 1$).

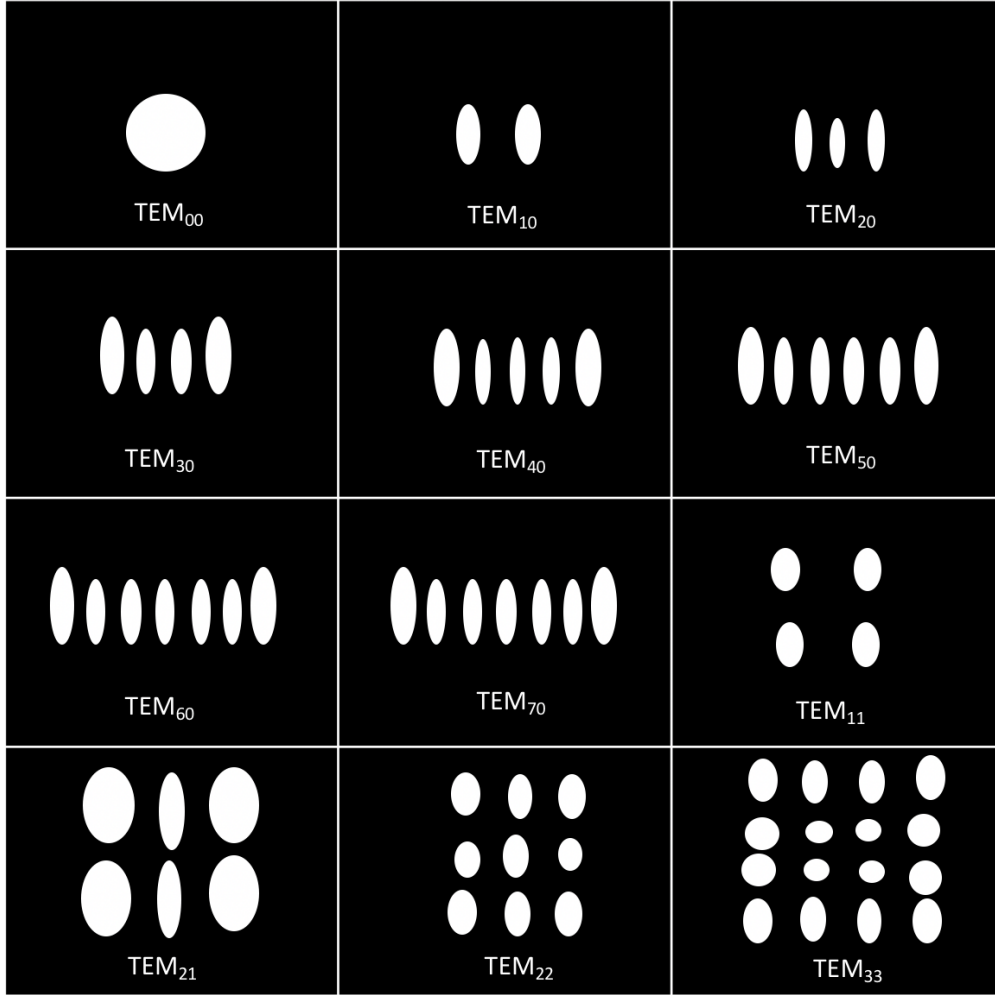


Figure 17: Some examples of transverse electromagnetic modes observed for a Fabry-Perot cavity.

For the case where a beam is spatially mode matched to the fundamental TEM_{00} mode (when the wave fronts of the Gaussian beam perfectly match with the mirror surfaces and the incoming beam is aligned to the optical axis of the resonator), no higher order modes are present. The distance between two consecutive TEM_{00} modes is called the free spectral range (FSR) of the resonator and is given by

$$\Delta\lambda_{\text{FSR}} = \frac{c}{2L}, \quad (27)$$

where L is the distance between cavity mirrors. For cavity mirrors having identical reflectivities, the free spectral range divided by the linewidth or full width at half maximum $\Delta\lambda_{\text{FWHM}}$ is given by the finesse,

$$F = \frac{\Delta\lambda_{\text{FSR}}}{\Delta\lambda_{\text{FWHM}}} = \frac{\pi\sqrt{R}}{1-R}. \quad (28)$$

Thus the finesse counts the number of different wavelengths distinguishable by the etalon. For an interferometer with two mirrors with different reflectivities, R_1 and R_2 , the finesse is given by

$$F = \frac{\pi(R_1R_2)^{1/4}}{1-(R_1R_2)^{1/2}}, \quad (29)$$

which represents the geometrical average of the two mirror reflectivities [2]. Some algebra provides a very useful equation for the linewidth,

$$\Delta\lambda_{\text{FWHM}} = \frac{c}{2L} \frac{(1-R)}{\pi\sqrt{R}}. \quad (30)$$

1.3.4 Pound Drever Hall Technique

One of the most widely used techniques for laser stabilization is the Pound-Drever-Hall (PDH) technique, which utilizes the resonances of a cavity and a feedback loop to keep a laser frequency relatively constant. "Out of the box" lasers are typically not stable enough for high-precision measurements and experiments, especially for those using spectroscopy or interferometric gravitational-wave detection. Similar to frequency modulation, a laser's frequency is modulated and results are fed back into a tunable laser to suppress changes in frequency.

In the most fundamental form, the feedback loop begins with the beam of a tunable laser that is modulated before entering a Fabry-Perot cavity. The modulated beam is reflected off of the cavity and enters a photodetector to measure the reflected intensity. The signal is then mixed down with a local oscillator and passed through a low-pass filter before entering

a servo amplifier or lock box which feeds the signal into the laser for frequency corrections.

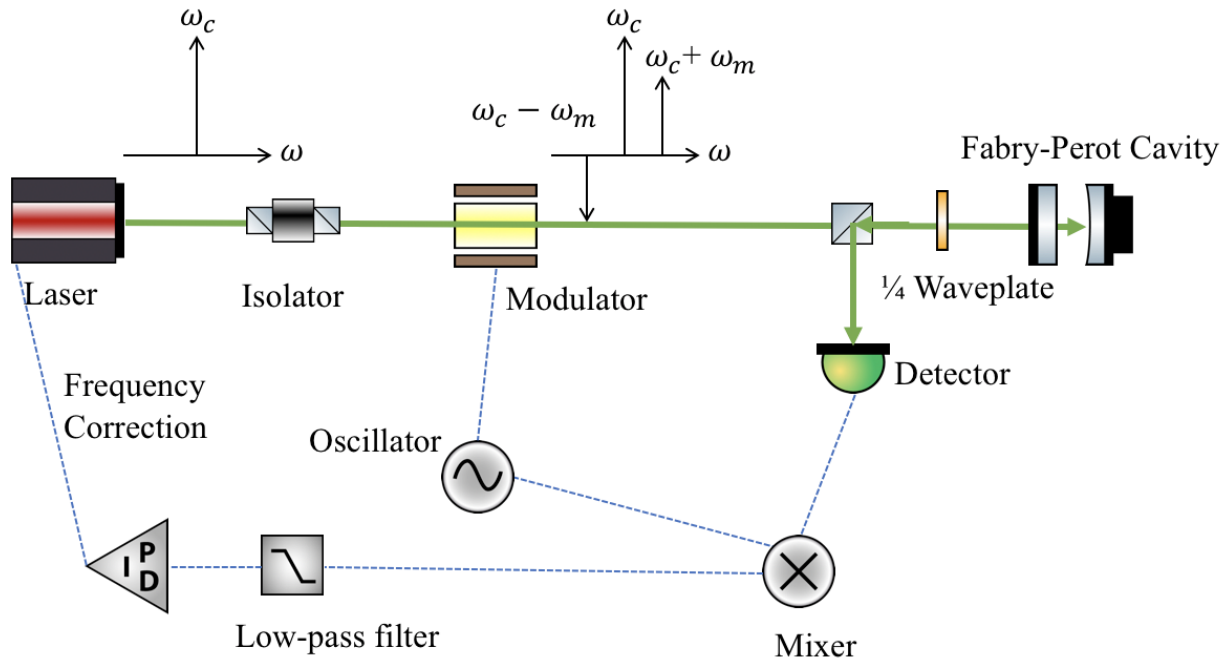


Figure 18: Layout for Pound-Drever-Hall laser stabilization. The beam of a tunable laser is passed through a modulator and then reflected off a Fabry-Perot cavity before being received by a photodetector. The signal from the photodetector is then mixed down with a local oscillator before a low-pass filter, which isolates the signal needed for an error signal.

For a simple yet practical setup, a beam of the tunable laser passes through an isolator to minimize any destabilization due to reflections entering back into the laser. The beam is then phase modulated, in our case using an electro-optic-modulator (EOM), which yields sidebands and a carrier beam. This modulation to generate sidebands is necessary for the PDH technique so there is a definite phase relationship between incident and reflected beams of the system. The modulated beam passes through another isolator in the form of a polarizing beam splitter and quarter-wave plate before reaching the Fabry-Perot cavity. The beam reflected off of the cavity is the sum of two coherent beams: one reflected off of the first mirror and a beam that passed through the first mirror to enter the high-finesse cavity. The reflected beam is received by a photodetector where there is interference to create a beat pattern. The phase of the pattern provides phase information about the reflected beam,

which allows the determination of whether the laser frequency is above or below cavity resonance.

The Error Signal

In the Pound-Dreave-Hall setup [1], where we have a carrier and two sidebands, the total reflected beam is

$$E_{\text{ref}} = E_0[f(\omega)J_0(\beta)e^{i\omega t} + f(\omega + \Delta\omega)J_1(\beta)e^{i(\omega+\Delta\omega)t} - f(\omega - \Delta\omega)J_1(\beta)e^{i(\omega-\Delta\omega)t}], \quad (31)$$

where J and $f(\omega)$ represent Bessel functions and Airy functions, respectively. β is known as the modulation depth. Since the photodetector is measuring power in the reflected beam, we use

$$P_{\text{ref}} = |E_{\text{ref}}|^2$$

to obtain

$$\begin{aligned} P_{\text{ref}} = & P_c|f(\omega)|^2 + P_s[|f(\omega + \Delta\omega)|^2 + |f(\omega - \Delta\omega)|^2 \\ & + 2\sqrt{P_c P_s} \text{Re}[f(\omega)f^*(\omega + \Delta\omega) - f^*(\omega)f(\omega - \Delta\omega)] \cos \Delta\omega t \\ & + \text{Im}[f(\omega)f^*(\omega + \Delta\omega) - f^*(\omega)f(\omega - \Delta\omega)] \sin \Delta\omega t + (2\Delta\omega \text{ terms})], \end{aligned} \quad (32)$$

where c stands for carrier and s for sideband in the equation. Here we have three waves of different frequencies: the carrier ω and the upper and lower sidebands at $\omega \pm \Delta\omega$. The result is a wave with nominal frequency of ω , but with an envelope displaying a beat pattern with two frequencies [1]. The key terms of interest are the oscillating terms at modulation frequency $\Delta\omega$ as they provide the phase of the reflected carrier. These terms are represented as sine and cosine terms.

Since the signal from the photodetector contains multiple terms that we are not particularly interested in, some isolation of the oscillating terms is necessary. This is performed by

sending the signal into a mixer and through a low-pass filter. A mixer essentially forms the product of its inputs, and the product of two sine waves is

$$\sin \Delta\omega t \sin \Delta\omega' t = \frac{1}{2} \{ \cos [(\Delta\omega - \Delta\omega')t] - \cos [(\Delta\omega + \Delta\omega')t] \}.$$

If we mix down the modulation signal $\Delta\omega$ and some other signal at $\Delta\omega'$, we can see the output will contain signals at both the sum and difference of the two frequencies. When they are equal, we are provided with part of the frequency signal we are interested in and can isolate a DC signal using a low-pass filter. This is the case for two in-phase signals going into the mixer. We can represent mixing down two out-of-phase frequencies as

$$\sin \Delta\omega t \cos \Delta\omega' t = \frac{1}{2} \{ \sin [(\Delta\omega - \Delta\omega')t] - \sin [(\Delta\omega + \Delta\omega')t] \}.$$

Here we see that the DC signal vanishes when the frequencies are equal, so if we want to measure the error signal when the modulation frequency is low, phases of the two signals going into the mixer must match. In a relatively slowly-modulated model, the instantaneous frequency for the phase-modulated beam [1] is

$$\omega(t) = \frac{d}{dt}(\omega t + \beta \sin \Delta\omega t) = \omega + \Delta\omega\beta \cos \Delta\omega t. \quad (33)$$

With the reflected power being $P_{\text{ref}} = P_0|f(\omega)|^2$, where P_0 is the power of the incident beam, and expecting it to vary over time it can be represented as

$$P_{\text{ref}}(\omega + \Delta\omega\beta \cos \Delta\omega t) \approx P_{\text{ref}}(\omega) + \frac{dP_{\text{ref}}}{d\omega} \Delta\omega\beta \cos \Delta\omega t \approx P_{\text{ref}}(\omega) + P_0 \frac{d|f|^2}{d\omega} \Delta\omega\beta \cos \Delta\omega t. \quad (34)$$

Since in the model of interest the frequency is being dithered slowly enough that the standing wave inside the cavity is in equilibrium with the incident beam, a comparable order of magnitude with cavity linewidth, we can approximate $\Delta\omega$ to be very small. This leads to

$$f(\omega)f^*(\omega + \Delta\omega) - f^*(\omega)f(\omega - \Delta\omega) \approx 2\text{Re} \left\{ f(\omega) \frac{d}{d\omega} f^*(\omega) \right\} \Delta\omega \approx \frac{d|f|^2}{d\omega} \Delta\omega, \quad (35)$$

which is purely real and only the cosine term survives. If we approximate $\sqrt{P_c P_s} \approx P_0 \frac{\beta}{2}$, the reflected power becomes

$$P_{\text{ref}} \approx \text{constant terms} + P_0 \frac{d|f|^2}{d\omega} \Delta\omega \beta \cos \Delta\omega t + (2\Delta\omega \text{ terms}). \quad (36)$$

Mixing will filter out everything but the term that varies as $\cos \Delta\omega t$. Therefore, the PDH error signal [1] is determined to be

$$\epsilon = P_0 \frac{d|f|^2}{d\omega} \Delta\omega \beta \approx 2\sqrt{P_c P_s} \frac{d|f|^2}{d\omega} \Delta\omega. \quad (37)$$

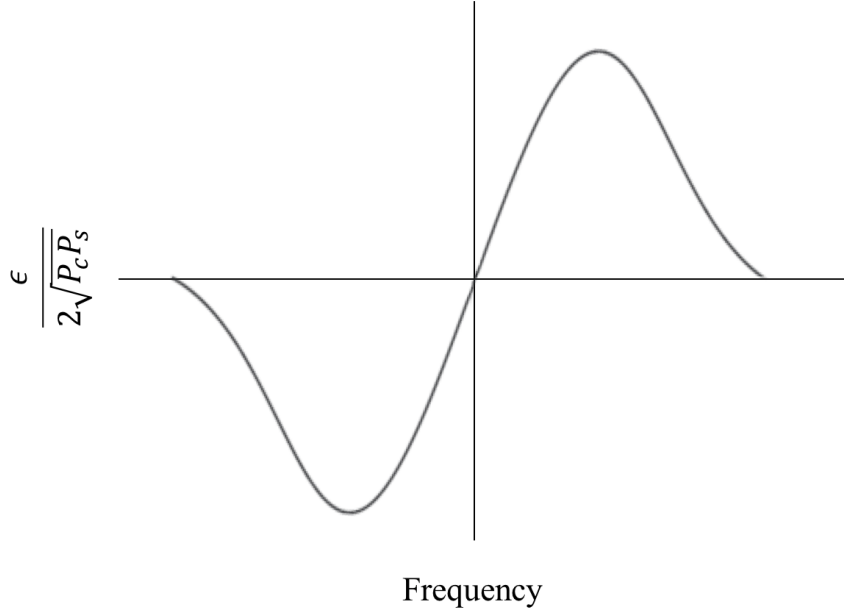


Figure 19: The form of Pound-Drever-Hall error signal when the modulation frequency is relatively-low.

2 Experimental Setup

2.1 Preparation

2.1.1 Innolume Gain Module

The external cavity laser (ECL) constructed provides a low-cost option for various applications in AMO physics and has beneficial characteristics of a single-angled-facet (SAF) gain chip. A significantly wider wavelength tunability and narrower spectral linewidth have been demonstrated for ECLs using SAF gain chips compared to conventional Fabry-Perot (FP) laser diodes, for which anti-reflective (AR) coating is only effective around the design wavelength [13]. In addition, SAF gain chips are usually constructed with extended active ridge lengths spanning a few millimeters, an order of magnitude longer than FP laser diodes, allowing reductions in injection current-induced frequency noise. Another notable advantage of SAF gain chips in an ECL configuration is the output beam-pointing stability from the normal facet, enabling a robust, fiber-coupled operation unaffected by adjustments on the Littrow angle [13].

The Innolume gain-module (GM-1060-150-YY-250) used is a gain-chip that has one side coupled into a single mode fiber and eliminates the need for various components typically used in devices with a bare gain-chip. This improves reliability and reduces costs associated with a more complex system, and is one of the reasons why we used the gain module as the source of the tunable laser. An additional appealing feature is the built-in TEC and thermistor, providing further temperature stability. The compact module has a central wavelength of 1060 nm with a tuning range width of 150 nm and maximum power at 1100 nm.

Typical ECL configurations are Littrow, which is applied to the system herein, and Littman/Metcalf cavities. For the Littrow configuration, a diffraction grating is mounted in a way that light of the desired wavelength is diffracted back along the incident beam, where wavelength is

scanned by rotating the grating. Generally an intracavity achromatic lens is used to collimate the expanded beam on a relatively large area of the grating. The setup used for this project is similar to the Littrow configuration such that the gain-module was mounted on a custom aluminum platform along with a mounted aspheric lens. The incident beam was collimated as it passed through the aspheric lens and the first-order diffracted beam was sent back along the incident beam to feedback into the module.

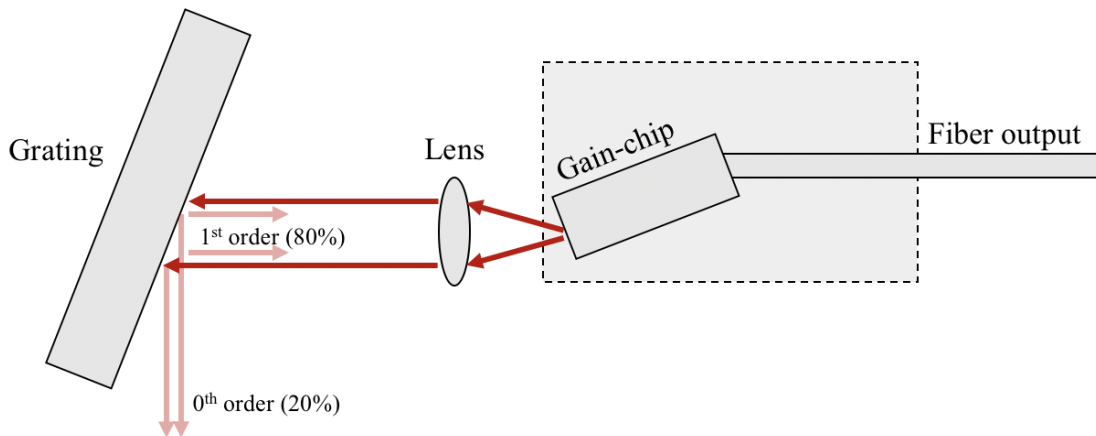


Figure 20: External cavity scheme used for device characterization, showing how the gain-chip is oriented within the module and grating positioning.

The gain-module device is constructed using a gain-chip that has a curved stripe, a deep AR coating at the tilted side, and a few-percent-reflection at the normal side. The wavelength selecting feedback has to be placed at the tilted side, whereas the output power goes out from the normal side. The facet where the stripe is tilted is designed for external feedback, resulting in low back-reflection to the chip waveguide [13].

Optimizing the Output

Once set up with a diode controller source and TEC, the gain module ECL system was adjusted to produce an infrared beam at approximately 1108 nm. The beam was collimated using an aspheric lens exposed to a kinetic mount and infrared viewing cards mounted to the wall at approximately 1.5 m from the gain module tilted side output.

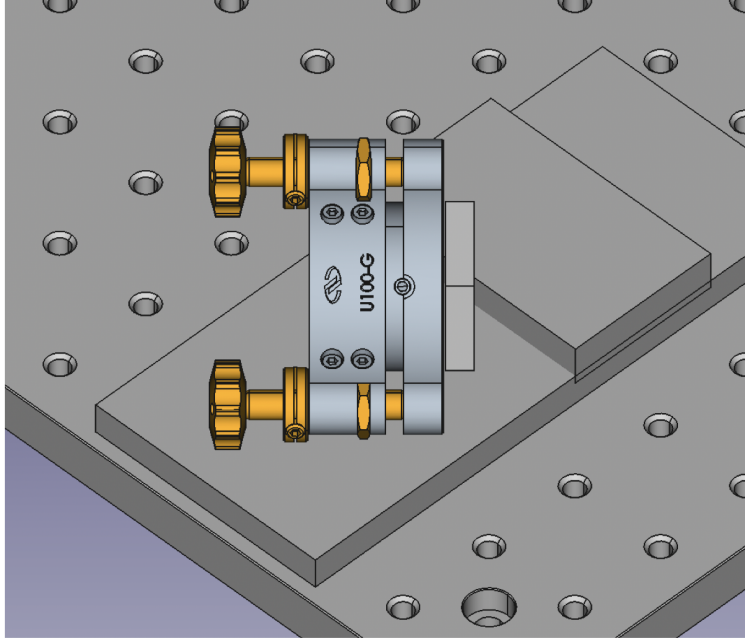


Figure 21: Rendering of the gain module and grating mount platforms for the external cavity gain chip laser system.

The blaze grating (Thorlabs GR13-1210) for the system was epoxied upon a 1-in pedestal pillar post (Thorlabs RS05P8E) and then secured into the clear aperture of a gimbal mount (Newport U100-G). The mount was then screwed into a custom raised platform to be centered in the vertical with the mounted aspheric lens. The distance between the aspheric lens and the grating was measured to be approximately 4 cm. Obtaining a substantial power output from the gain module fiber output took tuning of the grating in the form of manually finding a position of the grating that coarsely aligns the first-order diffracted beam with the gain module output and variations to the grating mount adjusting knobs. A viewing card with a pinhole was used to determine initial coarse beam alignment. The fiber output was connected to a power meter (Thorlabs PM100D) and monitored during grating adjustments. When power output was maximized, coarse current and TEC adjustments were made to optimize the beam intensity. This process was carried out to ensure all system components were working and that substantial beam power could be generated. Initial maximum beam power at 1108 nm was approximately 140 mW, however the output would later be optimized

at specific wavelengths of light and would yield different results; at one point reaching a maximum of roughly 200 mW of 1100 nm light. Initial calibration and testing of the gain module was done with current sweeps between 300 mA and 600 mA with a constant gain module TEC temperature of 29.865 °C during the initial current sweeps, which provided an expected linear relationship to output power. This brief demonstration served for calibration only and future adjustments to the grating position and gain module TEC temperature would be made to tune the output frequency to a desired value.

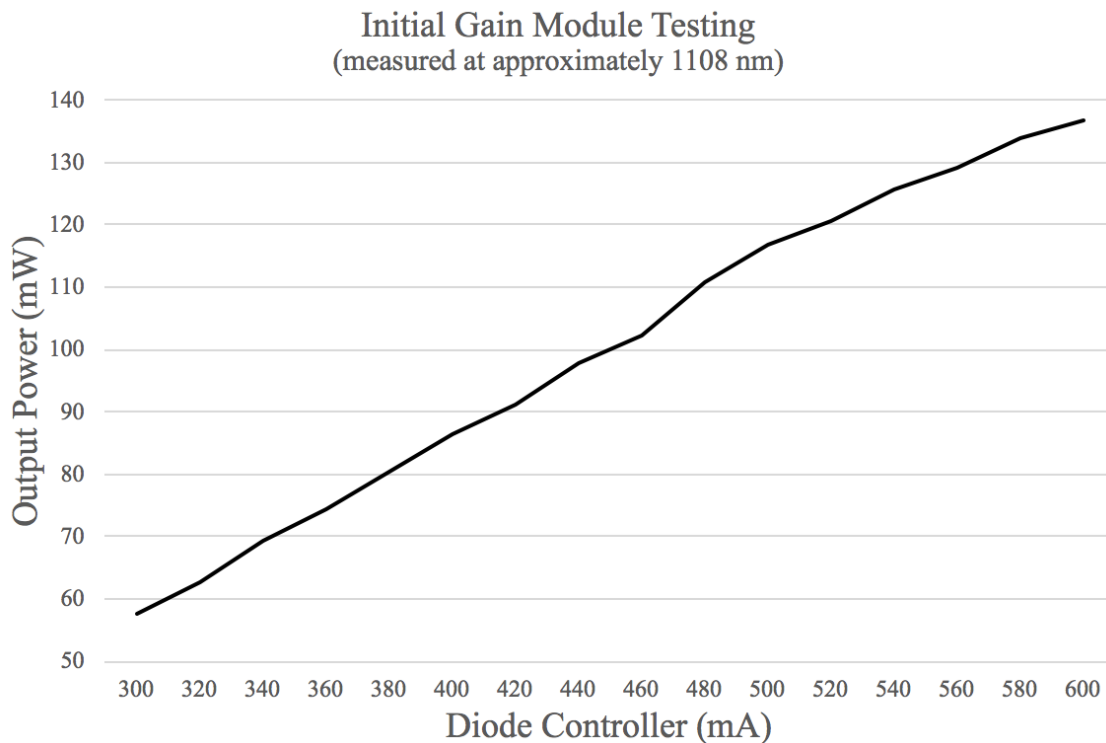


Figure 22: Initial testing and current sweeps for the gain module output showing a linear relationship.

Stabilization and Isolation

During additional testing and the preliminary setup for the Pound-Drever-Hall lock (to be presented in a subsequent section), a severe jitter in the error signal was discovered and it was realized there was an isolation issue with the gain module system. This was quickly addressed using four Sorbothane[®] vibration-absorbing feet under each corner of the small breadboard

housing the gain module system and a padded enclosure made of cushioning-foam cubed sheets. These additions drastically reduced the signal jitter and helped to provide a more stable temperature for the system components, as well as a clean error signal for locking.

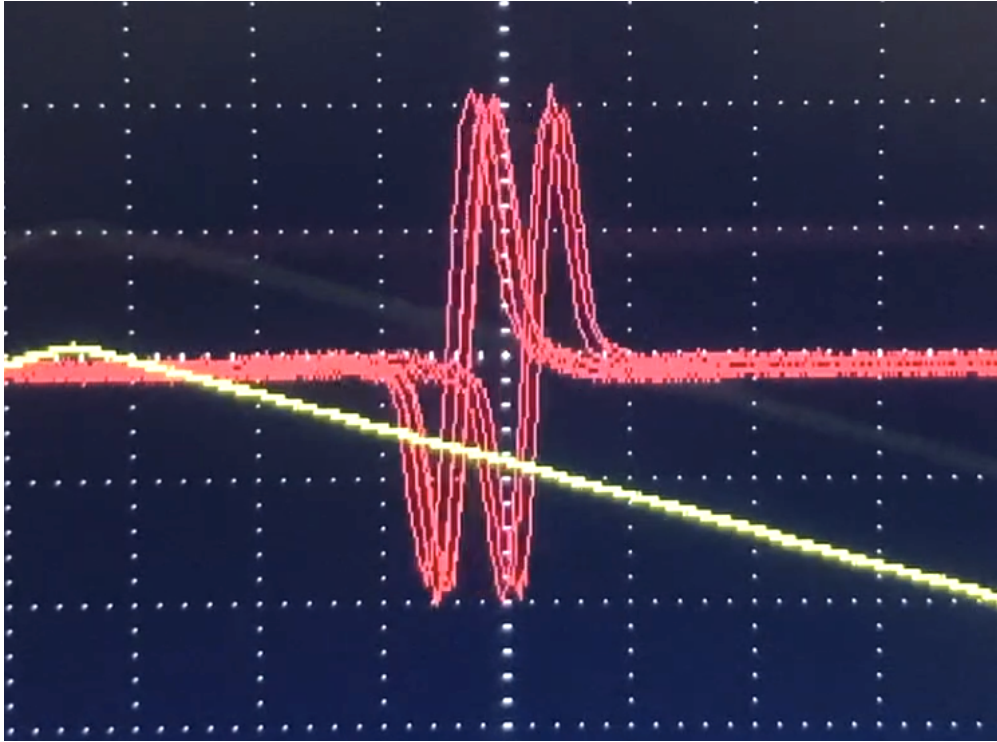


Figure 23: The initial PDH error signal showing a severe jitter and unstable signal, where the signal has a voltage division of 10.0 mV. The width of the graphic is ~ 6 MHz and the yellow line is a sweep signal of 140 kHz.

2.1.2 Cavity Design

For the Pound-Drever-Hall stabilization component of the system, a Fabry-Perot interferometer was fabricated using 32-5 Super Invar. The material is a low expansion alloy composed of roughly 32% nickel and 5% cobalt, iron, and trace amounts of other metals and minerals like copper, aluminum, and manganese. The appealing characteristic of Super Invar is its minimal susceptibility to thermal expansion under room-temperature conditions, as well as fewer thermal expansion properties at higher temperatures than standard Invar.

The two-mirror cavity design was chosen to be a semiconfocal resonator and based on previous constructions that have shown consistent success [12]. A Noliac/CTS (NAC2123) piezo ring actuator was used to assist with laser frequency correction, which is 12 x 6 mm with a free stroke of 3.3 μm and a blocking force of 3560 N. Two Thorlabs SM05LTRR stress-free retaining rings were placed within each side of the cavity, securing a plano-concave mirror-piezo stack on one side and a single mirror on the other. The mirrors were provided through Laseroptik with each respectively being the L-16895 (plano-concave, $R_1 = -500$ mm) and the L-16896 (plane), both with a reflectivity of 99% for wavelengths between 400 and 650 nm.

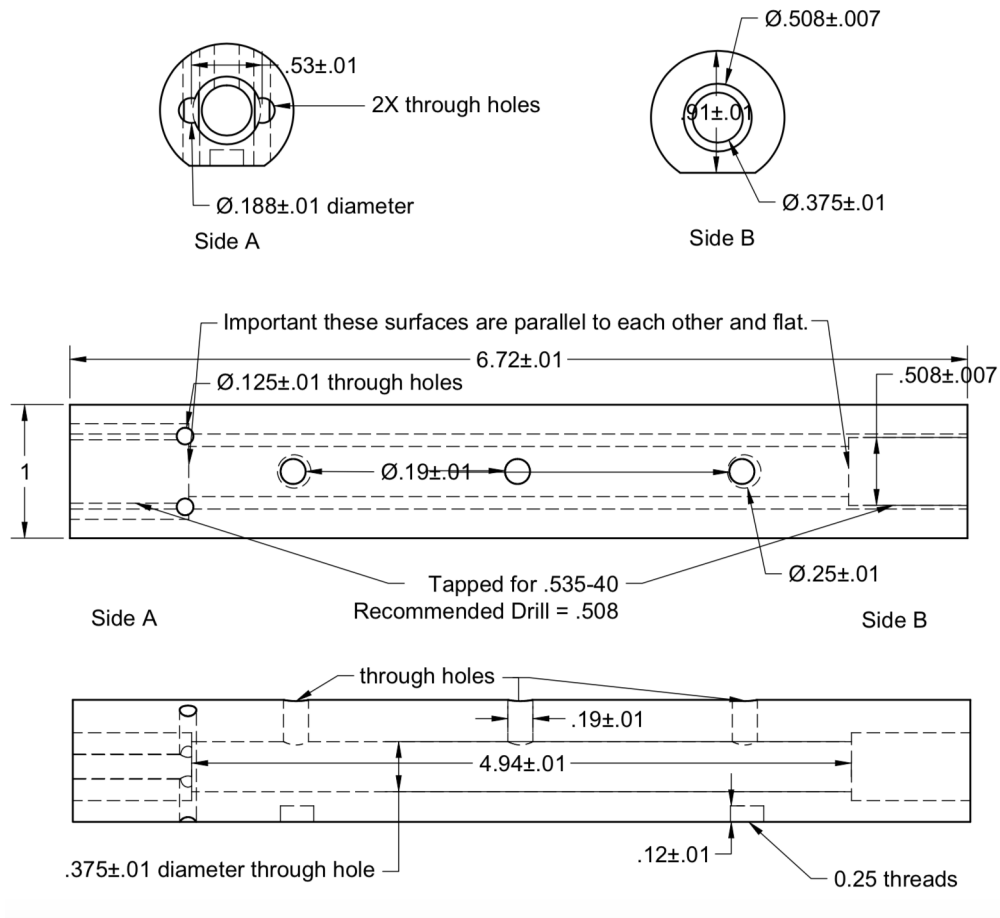


Figure 24: Diagram for the Fabry-Perot cavity used as part of the application of the PDH technique for frequency stabilization. Measurements are in inches.

Using the known cavity length, the beam waist [16] was calculated to be

$$\omega_0^2 = \frac{\lambda}{2\pi} \sqrt{L(r-L)} \rightarrow \omega_0 = 138 \mu\text{m}, \quad (38)$$

where λ is the wavelength of 554 nm, L is the cavity length of 0.125 m between mirrors and r is the radius of curvature of 500 mm. To be complete, the free spectral range, finesse, and linewidth were found to be

$$\lambda_{\text{FSR}} = \frac{c}{2L} = 1.20 \text{ GHz}, \quad (39)$$

$$F = \frac{\pi\sqrt{R}}{1-R} = 311, \quad (40)$$

$$\lambda_{\text{FWHM}} = \frac{\lambda_{\text{FSR}}}{F} = 3.86 \text{ MHz}, \quad (41)$$

where R is the reflectivity of the mirror.

To determine the total distance to focus the beam to, a simple equation for linear magnification of a thin lens can be used:

$$M = \frac{y_2}{y_1} = -\frac{s_2}{s_1} = \frac{f}{f-s_1} \Rightarrow \frac{s_2}{s_1} = \frac{s_1-f}{f}, \quad (42)$$

$$s_1 = \frac{y_1}{2y_2} f + f = 0.760 \text{ cm} = 0.00760 \text{ m}, \quad (43)$$

$$s_2 = \frac{2y_2}{y_1} s_1 = 60.0 \text{ cm} = 0.600 \text{ m}, \quad (44)$$

where y_1 represents the fiber mode field diameter of $\approx 3.50 \mu\text{m}$, y_2 is equivalent to the beam waist of $138 \mu\text{m}$, and s_1 and s_2 are the distances from the beam to the lens and object, respectively. In equations (43) and (44) the factor of 2 arises for the fiber mode field radius. f represents the focal length of the lens. A visual representation of the magnification equation is shown in Figure 25.

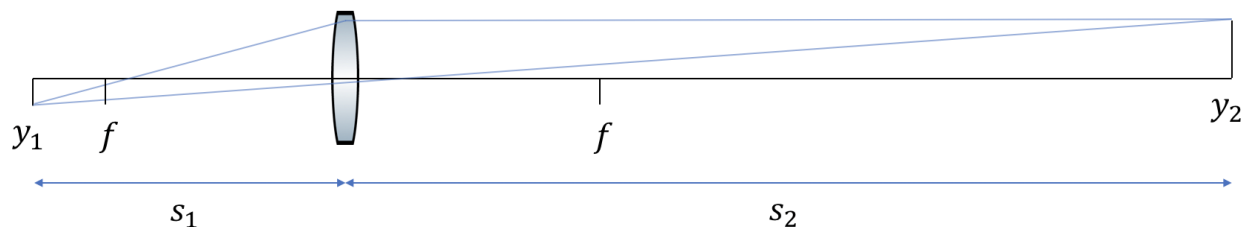


Figure 25: With an equation for magnification, one can determine the total distance to focus to when aligning a scanning Fabry-Perot cavity.

Using the calculated distance, the basic optical setup for the Fabry-Perot cavity and alignment for the PDH lock is represented in Figure 26, showing respective distances measured in between each optical component.

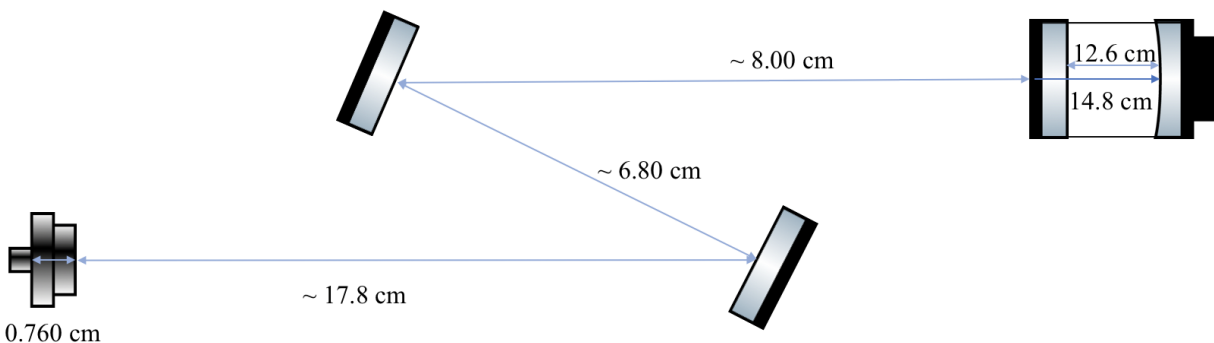


Figure 26: The basic optical setup for the Fabry-Perot interferometer was completed using the focal distance determined by the equations for magnification.

Once a beam is coarsely adjusted so that it is aligned with the mirrors and into the center of the cavity, the next step is to seek a faint transmission of the beam on the back end or opposite side of the cavity. This was done using a focusing lens and a video camera connected to a small monitor to make viewing easier. These components are unnecessary to complete the task of alignment and observing cavity modes as the transmission can be viewed on a card, however it will be quite small. Once the beam has been aligned so there is some transmission on the back end of the cavity, the mirrors can be adjusted using a "walking the beam" method until a ring can be observed. Further mirror adjustments are to be made until the beam has been "walked" into a singularity or dot, leading to various

cavity modes blinking in and out of view in the small area of the beam transmission. With this task complete, the cavity has been aligned.

To further test the cavity in preparation to use as part of the PDH component of the system, one can set up one or more photodetectors for viewing (setup provided in the subsequent section) cavity modes on an oscilloscope. Doing so allows experimental measurements of free spectral range and linewidth.

2.1.3 AdvR Fiber Modules

A necessary part of the contribution to the project presented herein was frequency conversion and phase modulation to lock an 1108 nm pump laser to an iodine reference. AdvR, a recognized leader in the engineering of nonlinear optical structures for a host of photonic devices and applications, was a key partner in the application of second harmonic generation and frequency modulation.

AdvR SHG

The AdvR-designed SHG is a Fiber-In / Fiber-Out module (RSH-M0554-P98P48AL0) constructed to frequency-double an 1108 nm beam to yield a 554 nm beam used for the PDH lock and iodine reference lock of the system. The device combines quasi-phase matched second harmonic generation and phase modulation into a single fiber coupled waveguide. The FC/APC input and output fibers are PM980 and MP480, respectively.

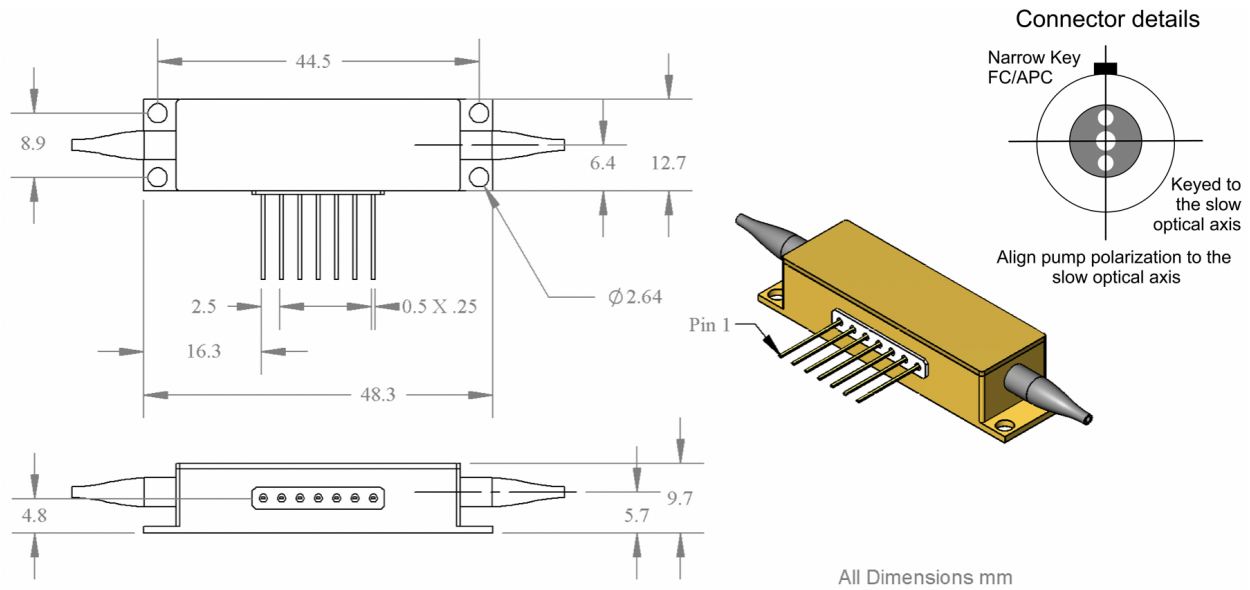


Figure 27: AdvR-designed SHG module used for second harmonic generation of a 554 nm beam incident upon the system discussed herein. Image provided courtesy of AdvR, 2021.

AdvR EOM

AdvR has developed a phase modulator in a KTP waveguide to operate in wavelengths ranging from near-infrared to near-ultraviolet, where the device used in this experiment is designed for the operational wavelength of 554 nm. The modulation frequency used for the PDH component of the system was 5 MHz, however this module can accommodate upwards of 6 GHz. The FC/APC input and output fibers are both PM480.

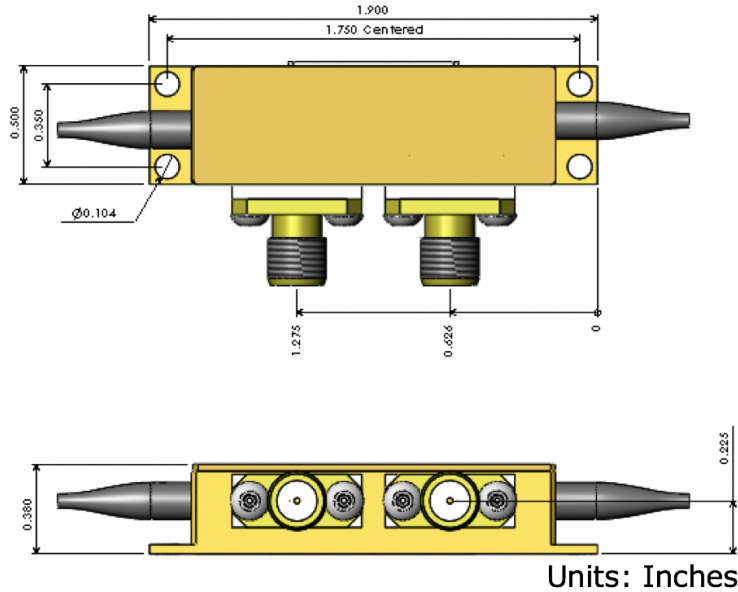


Figure 28: AdvR EOM used for frequency modulation of the incident beam upon the PDH lock. Image provided courtesy of AdvR, 2021.

2.1.4 IntraAction AOM

For this experiment, the IntraAction Model ATM-2002DA1 AOM was used. It is a Bragg diffraction device designed to be used as a laser beam intensity modulator, or in a limited sense as a laser beam deflector. Crystal Tellurium Dioxide (TeO_2) is used for the interaction medium and Lithium Niobate piezoelectric transducers are used to generate the RF frequency, longitudinal waves, and traveling acoustic waves inside the TeO_2 [3].

The RF center frequency is at 200 MHz and the active aperture (height of the sound field) is 2 mm. This model includes a soft multi-layer dielectric AR coating designed for operation between 440 nm and 700 nm. To optimize the diffraction efficiency during operation, the optical beam was aligned to the sound field and adjusted vertically to ensure that the total optical beam is in the sound field. For the setup presented, the system utilizes a double-pass AOM technique where the beam enters the modulator to produce a high-intensity first-order diffracted beam with the modulation, which is then isolated and reflected to pass back

through the AOM and into the system to serve as the modulated pump beam. This technique essentially eliminates changes in beam alignment during frequency sweeps and changes in frequency tuning of the AOM. The driving frequency was tuned to 160.1 MHz (applied to each beam pass) using a VCO (Mini-Circuits ZX95-200-S+) with 10.1 V into the V_{cc} and an equivalent 10.1 V into the V_{tune} ports. Using a bias tee (Mini-Circuits ZFBT-4R2G+), the VCO output and an additional dithering frequency of 90.0 kHz was sent through a series of amplifiers before meeting the AOM input. The AOM was mounted on a kinetic optical mount and adjusted to produced diffracted orders and ultimately finely-tuned for a high-intensity first-order diffracted beam.

2.1.5 Optics

The initial general optical design of the iodine transition lock component of the system, where modulation transfer spectroscopy is utilized, included a 90:10 beam splitter that sends the stronger pump beam around the system and into the double-pass AOM component, and polarizing beam splitters that ultimately allow intensity tuning of the pump and probe beams throughout the system. Following the beam path in Figure 29 and referencing components via Thorlabs: the incident beam at 554 nm is fiber-coupled through a FiberPort Collimator / Coupler and passes through a 10 mm polarizing beamsplitter cube (PBS101) before being directed into a quarter wave plate (WPQ05M-561) and half wave plate (WPH05M-561). The beam then gets split using a 90:10 non-polarizing cube (BS070), yielding a pump of 90% and probe of 10%. With standard protected silver mirrors (PF10-03-P01-10), the pump beam is sent around the system through another quarter wave plate and polarizing beamsplitter cube to serve as an optical isolator. The pump beam continues into the double-pass AOM component of the system before entering an additional polarizing beam splitter prior to reaching the iodine reference cell. The probe beam passes through a series of lenses (LA1509-A-ML and LA1608-A-ML) and an absorptive neutral density filter (NE05A) before being directed into the iodine cell, and ultimately into the photodetector (PDA10A2).

Both overlapping pump and probe beams were eventually focused down to a beam waist of $< 400 \mu\text{m}$ and approximately-collimated prior to passing through the iodine reference cell. Additional details and electronics regarding the optical engineering of the iodine system are presented in a subsequent section.

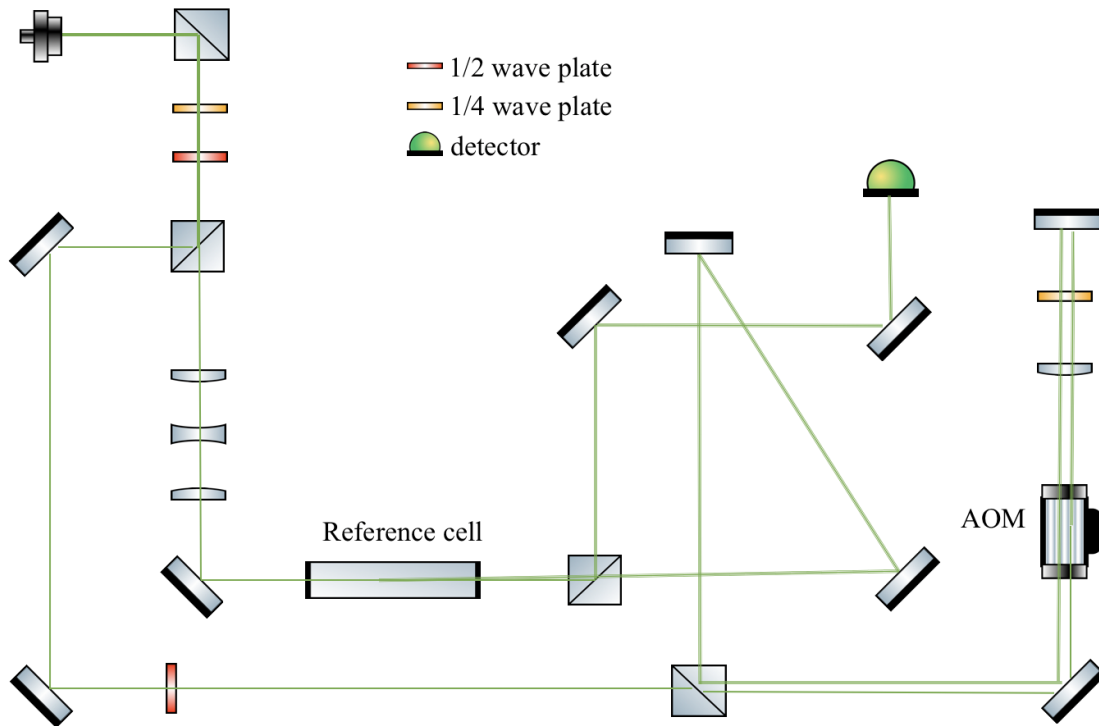


Figure 29: Shown is the initial optical setup for the iodine component of the system and where modulation transfer spectroscopy occurs. This served to be an excellent starting point for initial testing, however a redesign of the optics to increase beam intensity and pump-probe overlap would be necessary.

2.1.6 Iodine Vapor Cell

The 10 cm iodine ($^{127}\text{I}_2$) vapor reference cell used was provided by Thorlabs (GC19100-I). It is a quartz cell that features UV fused silica windows which are angled to compensate for beam offset and designed with a 2° wedge to eliminate etalon effects. The quartz reference cell also has a high-heat threshold up to 800°C .

The iodine vapor cell was held at room temperature (approximately 21 °C) for the duration of the testing and data collection presented herein, and covered with a dark foam for isolation; however it is noted that further isolation may help with stability and the success rate of lockable error signals in a given frequency region. Alignment techniques to ensure pump-probe beam overlap are of imperative importance.

2.1.7 High-Speed Servo Controller

The high-speed proportional integral (P-I) controller used (New Focus Model LB1005) has an intuitive front panel for the independent control of the P-I corner frequency, overall servo gain, and low-frequency gain limit. This flexibility enables the controller to link with other units for the high-speed control of diode lasers using both piezo-electric transducers and current modulation inputs [8].

Feedback (or servo) control forces a system, such as a laser, to stay actively locked to a specific frequency while correcting for external perturbations that might cause the system to deviate from the desired value. The servo controller provides critical signal-processing electronics for performing the feedback control. In the case of frequency locking, an error signal is generated by transmitting a portion of the laser output through a reference such as the cavity or vapor cell used herein. Frequency instabilities are converted to an amplitude change that can be detected by a photodetector. The resulting error signal is filtered by the servo controller to form a control signal that is sent back to the laser or cavity piezo.

The LB1005 Servo Controller consists of three stages [8] of analog electronics processing:

Input Stage: The input section is a difference amplifier with an adjustable voltage offset. Common-mode voltages ranging from ± 10 V can be subtracted. Error signals that exceed the voltage range ± 330 mV saturate the filter amplifier.

Filter Stage: This section converts the error signal to a control signal with a proportional-integral

(P-I) filter. Front panel controls adjust the overall loop gain, the P-I corner frequency, and an optional low-frequency gain limit. A toggle switch is used to disable/enable the output of the P-I filter for acquiring a lock.

Output Stage: The output section is a summing amplifier that adds the P-I control signal to other auxiliary signals, such as external sweep and modulation inputs.

2.2 Application of PDH Technique

2.2.1 Setup

The optical setup for a PDH lock is rather simple with efficacy strongly dependent upon the cavity design and beam alignment. As shown in Figure 30, the basic setup for the beam path included two mirrors, a polarized beam splitter, a quarter-wave plate, and the custom designed Fabry-Perot cavity. The gain module output of ~ 90 mW at 1108 nm had a custom fiber-spliced isolator by Oz Optics (FOI-21-11-1110-6/125-P-50-3A3A-1-1-35-SP) with output fiber-coupled to a 99:1 splitter with 1% being used to monitor frequency with a calibrated wave meter and the 99% entering the fiber AdvR SHG. The frequency-doubled beam output was ~ 10 mW and split using an additional 75:25 fiber-coupled splitter.

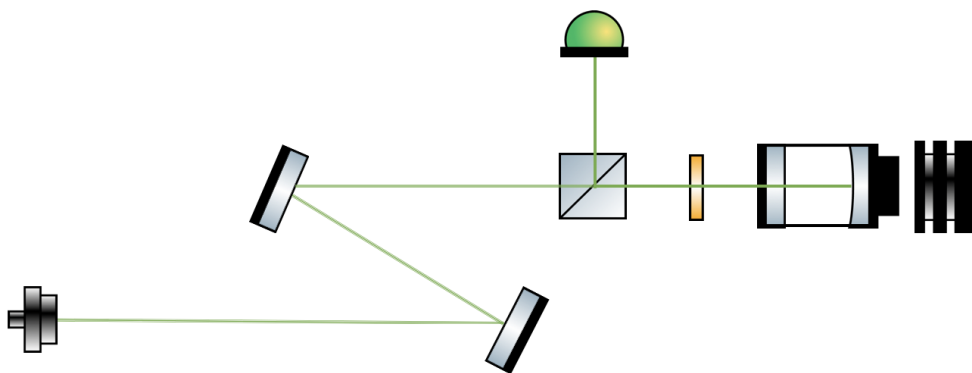


Figure 30: The basic optical setup for locking to a cavity via the PDH technique.

The 75% output was sent to the iodine component of the system, with the 25% output

being fiber-coupled into the AdvR EOM before entering the PDH lock. The modulator was fiber-coupled to a Thorlabs FiberPort Collimator / Coupler prior to reaching the mirrors. The EOM provided a modulation of 5 MHz in the form of a sine wave via a function generator and the adjustable FiberPort with five degrees of freedom made for a simplified way of focusing the beam to a magnitude comparable with the calculated beam waist of $\sim 138 \mu\text{m}$ for the Fabry-Perot cavity. As previously outlined generally, the photodetector signal and the function generator modulation frequency are mixed together and sent through a low pass filter of 1.9 MHz into the Newport LB1005 High-Speed Servo Controller to generate an error signal to eventually lock to.

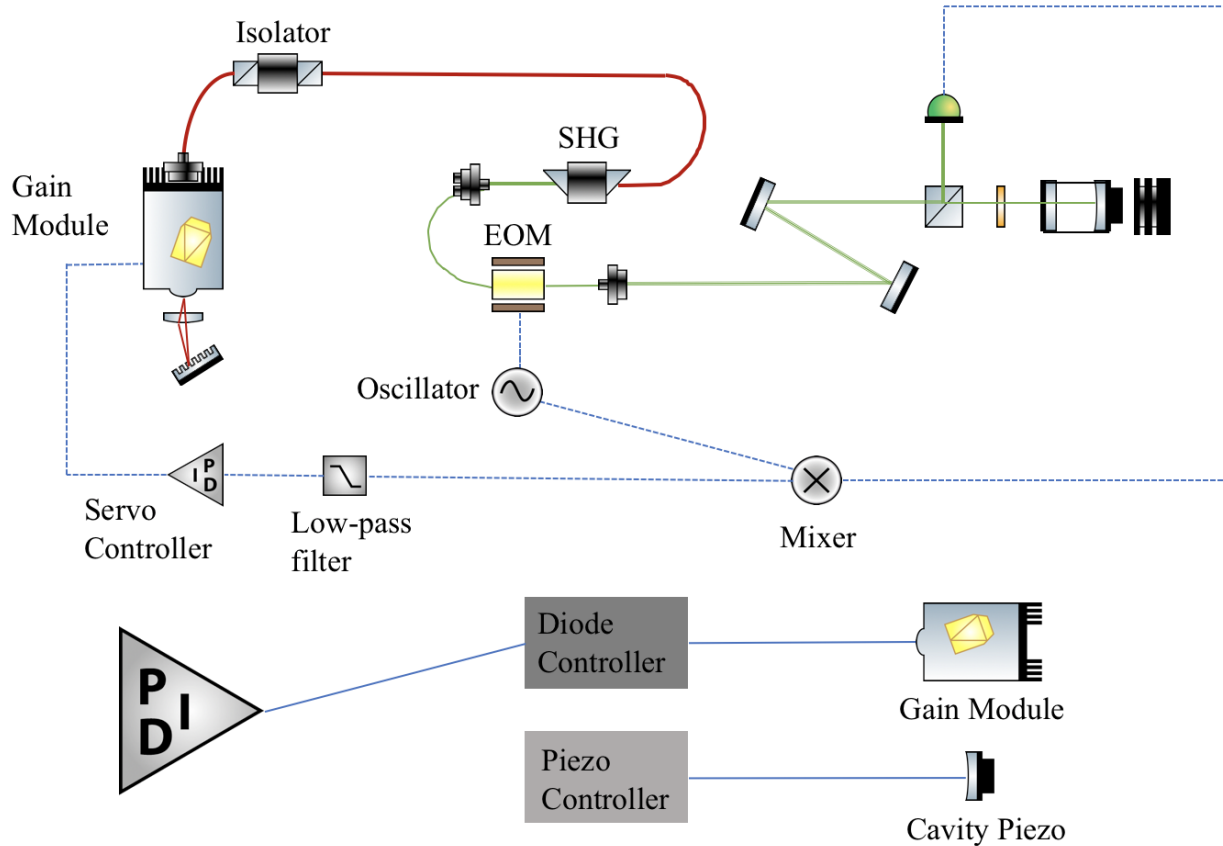


Figure 31: The PDH lock and fundamental electronics are shown, with the servo controller feeding back directly into the diode controller for coarse current sweeps in this case.

The servo controller output signal or feedback was sent to the gain module diode controller

for adjustments of frequency via coarse changes in current to the laser. It will be mentioned in the subsequent section for locking to an iodine reference that an additional servo output will be linked to the cavity piezo controller when locking to the iodine reference.

2.2.2 Observing Cavity Modes

After incorporating additional components within the initial Fabry-Perot cavity setup for the alignment procedure, there may be a need to finely tune mirror positions to ensure cavity modes are being observed in beam transmission occurring at the back end of the cavity. Once this is adjusted, it is a good check to connect the photodetector directly to an oscilloscope as this will provide better visual evidence of cavity modes being scanned by the cavity and a way to confirm calculated measurements made for the Fabry-Perot cavity. Ideally for most setups, there will be two photodetectors used - one to send to the mixer and another to be sent to an oscilloscope for viewing of cavity modes.

When searching for and viewing cavity modes on the oscilloscope, there are two parameters which can be adjusted outside of manually tuning mirrors in this setup: voltage to the cavity piezo and current to the gain module, which adjust cavity length and laser frequency. Adjusting each will allow for tuning sweeps to take place in search of specific cavity modes. Once it is clear the alignment and tuning efforts are adequate to provide cavity modes on the oscilloscope, locking to an error signal is just a few steps away.

2.2.3 Locking to an Error Signal

Once the Fabry-Perot cavity has been aligned and cavity modes are consistently observable, the signal of the photodetector for the reflected beam is sent into the mixer along with the same oscillator frequency of 5 MHz driving the EOM. A phase shifter may be required for any frequency offset at lower frequencies, however phase adjustment was unnecessary as there was no evident issue with a lag in phase as the error signals were ideal and clean. The mixed

signal then passes through the 1.9 MHz low-pass filter to assist with isolating an error signal, which enters the servo controller. For this setup, the sweep signal on the servo controller was driven with a function generator at 140 kHz. Using the sweep and parameters of current and a constant cavity piezo voltage of 39.000 V, steep dispersive error signals for the TEM₀₀ mode were found and the laser was locked to the cavity.

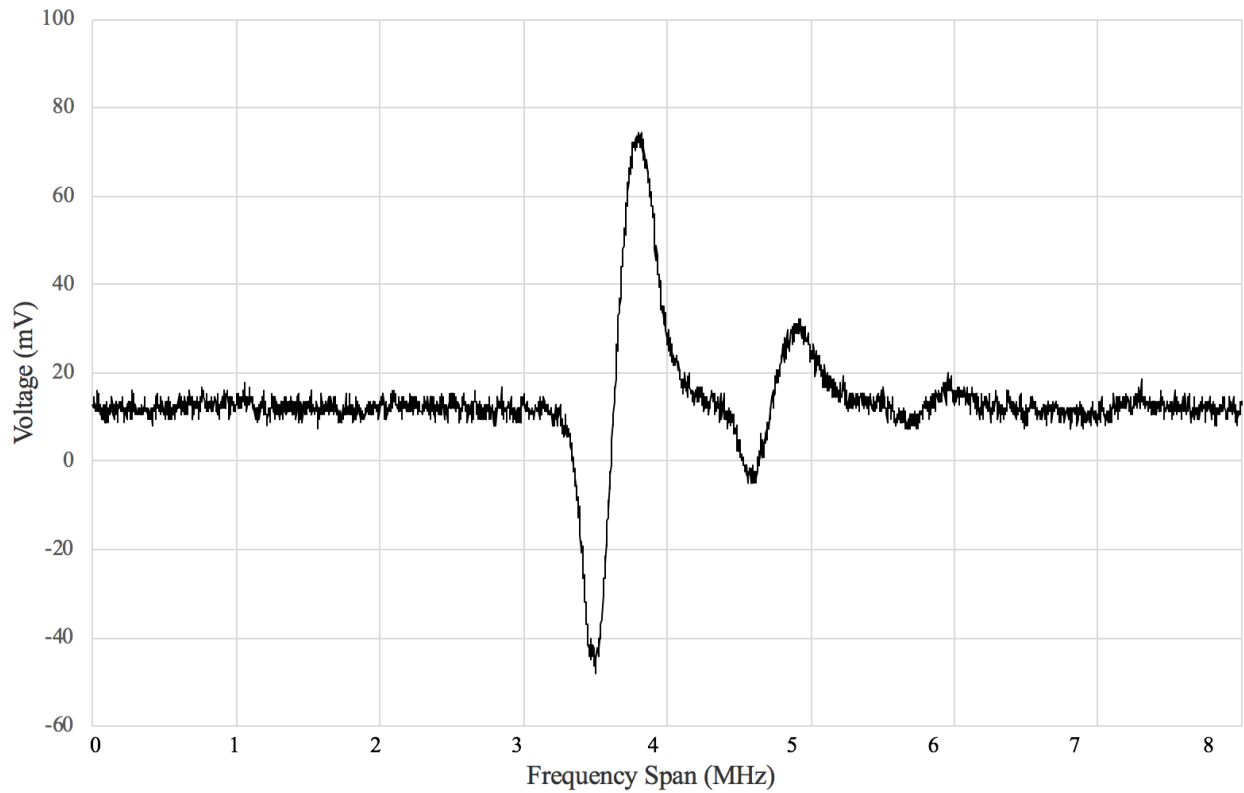


Figure 32: An example of a clean error signal obtained while locking frequency to the Fabry-Perot cavity using the PDH technique.



Figure 33: Screen capture from the video camera used on the output of the Fabry-Perot cavity while locking to the TEM₀₀ mode.

This served to be quite stable, and could remain locked with stability on the order of < 10 MHz for hours among ambient vibrations and nearby experiments. Figure 34 provides a comparison made between an unlocked and locked laser, while the subsequent graphic shows the lock stability over a longer duration.

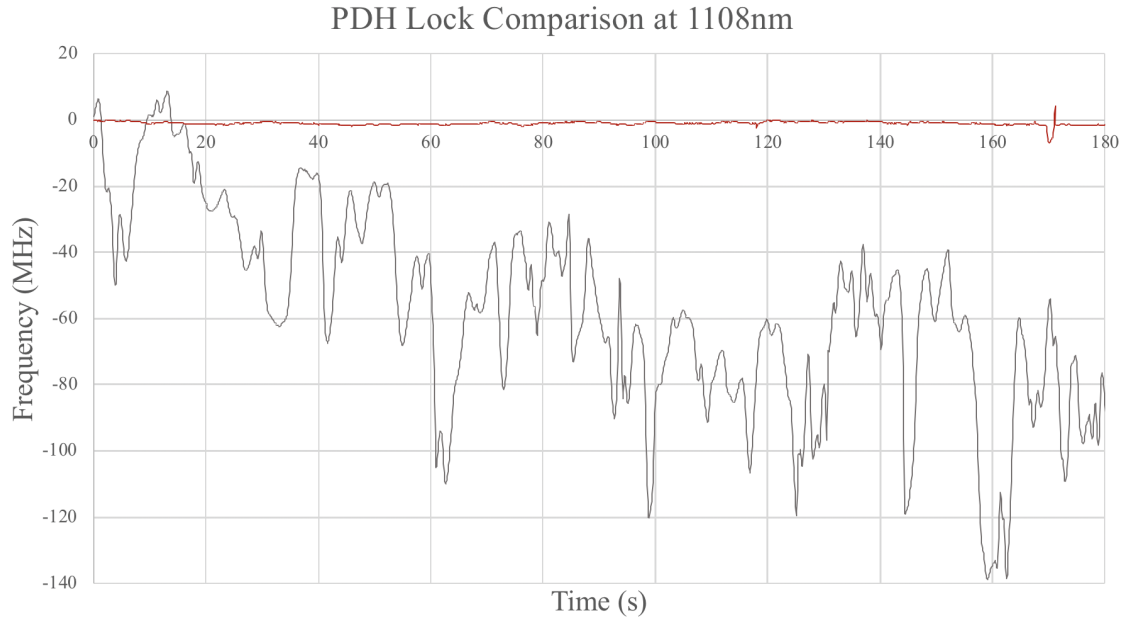


Figure 34: Initial demonstration of the working PDH lock in comparison to an unlocked gain module output, showing successful frequency stability. The red line represents frequency when the PDH lock is active while the black plot is the 1108 nm beam with no lock applied. The spike near the end of the locked signal was due to the laboratory doors being opened and shut, to be addressed in a subsequent section.

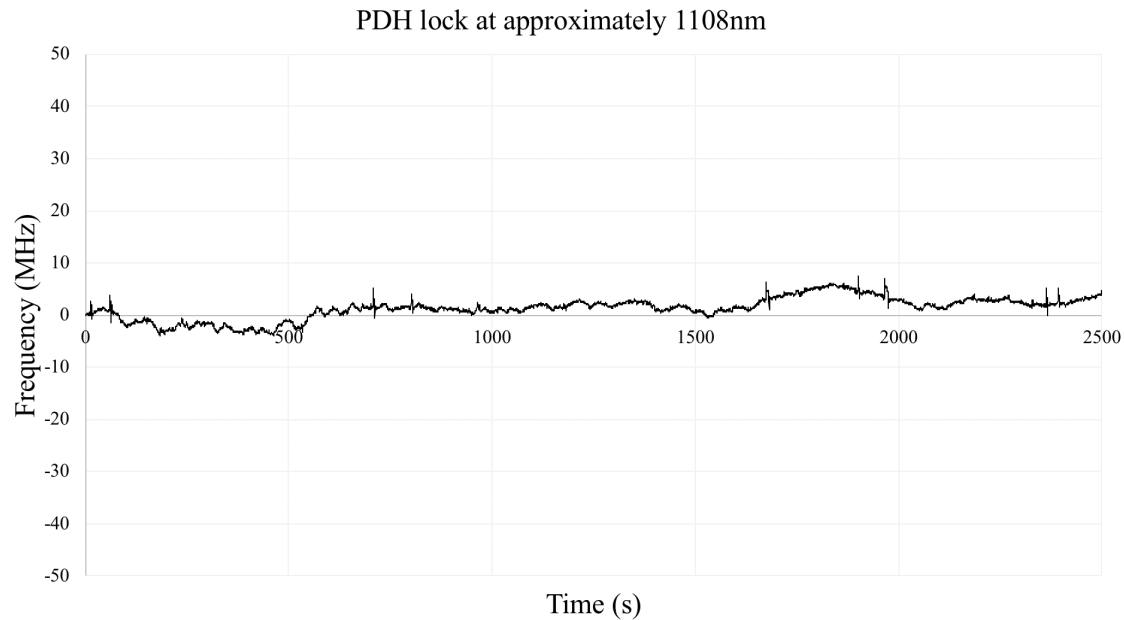


Figure 35: Frequency stabilization with an active PDH lock showing a maximum deviation of < 6 MHz during an interval over 40 minutes.

2.3 Locking to an Iodine Reference

2.3.1 Getting on Resonance

The respective pump and probe beam paths were aligned with efforts to minimize power loss and maximize the overlap of the beams within the iodine vapor cell. This was done using a semi-transparent card that allowed to view both beams on each side of the card as they were walked until the beams overlapped on both sides of the vapor cell and throughout the system, checking overlap at various stages. This technique is similar to using two irises or pin holes, with one on each side of the vapor cell, and tuning each respective beam to pass through both of the extremely small-diameter openings. With all of the optics discussed herein in place, an initial test of the beam and iodine cell is to get the laser tuned to hit iodine lines or in other words, on resonance. One telling sign that the laser is on resonance in this frequency region is visible fluorescence. The fluorescence will appear as a bright line inside of the vapor cell, but is not to be confused with scattering taking place at the faces or windows of the cell. Once fluorescence and ultimately resonance is obtained, it is useful to compare a photodetector signal with the respective region in the absorption spectrum.

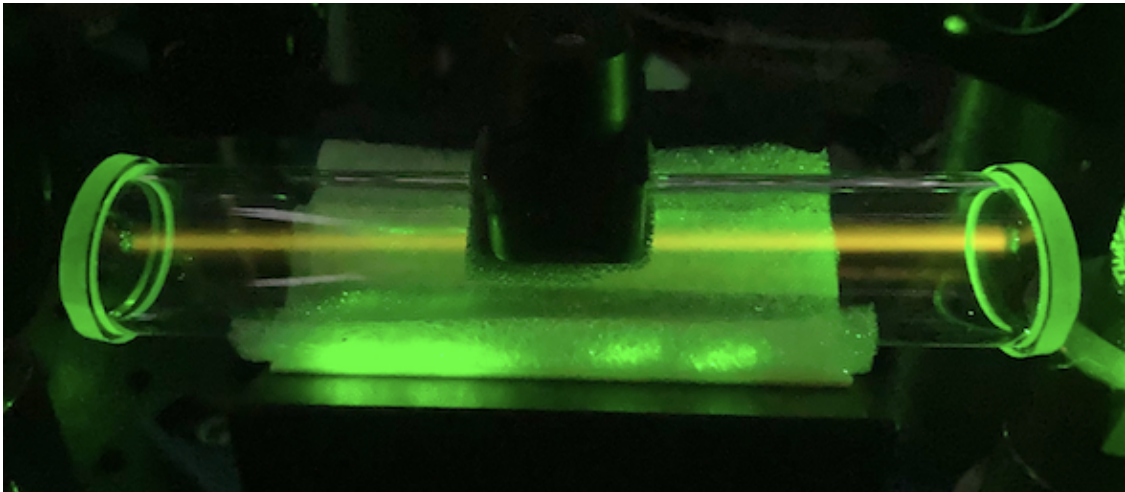


Figure 36: Observed fluorescence inside the iodine vapor cell during frequency sweeps. The shifted green absorption to yellow emission is characteristic of a Stokes Shift of ~ 25 nm.

Due to the importance of observing fluorescence, it is worth noting the cause of the yellow emission due to the Stokes Shift [21]. The phenomenon can be represented in an energy diagram as an initial excitation to a higher vibrational level followed by a rapid decay to the vibrational ground state, which yields fluorescence with a lower energy than the absorbed photon and therefore a longer wavelength. Intensity of a transition is determined by the population difference between initial and final states, where the transition probability between states which can be calculated using the Franck-Condon principle [15]. In classical terms, the Franck-Condon principle states that an electronic transition occurs without changes in the position of the nuclei of the molecule. This statement holds since nuclei are much more massive than electrons and therefore move relatively slow in comparison to rapid electronic transitions; and when excited, the sample initially has a non-equilibrium separation of the nuclei which then must relax back to equilibrium positions.

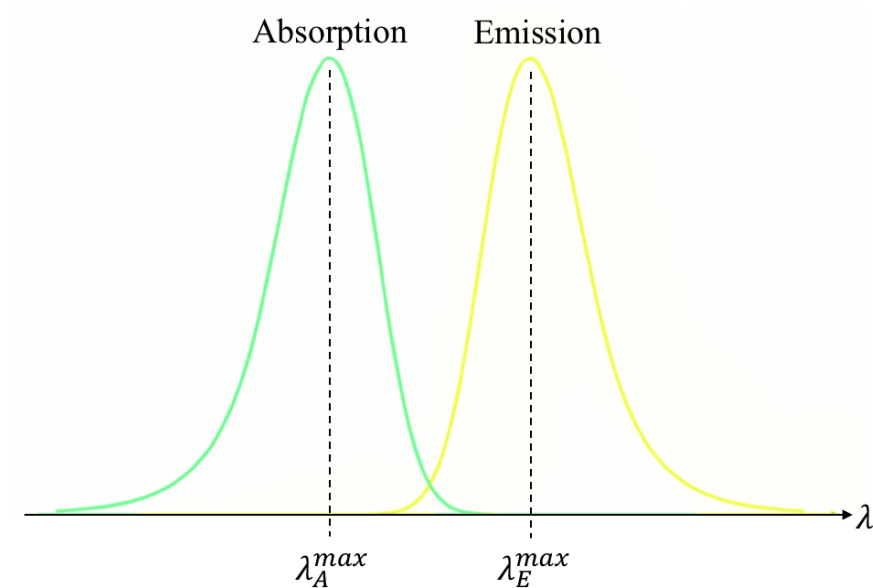


Figure 37: The Stokes shift is the difference between the spectral position of the maximum of the first absorption band and the maximum of the fluorescence emission.

For this experiment, fluorescence was initially observed at a frequency of 541.0840 THz corresponding to a wavelength of 554.0590 nm. Figures 38 and 39 show the section of the

iodine transmission spectrum where this is located.

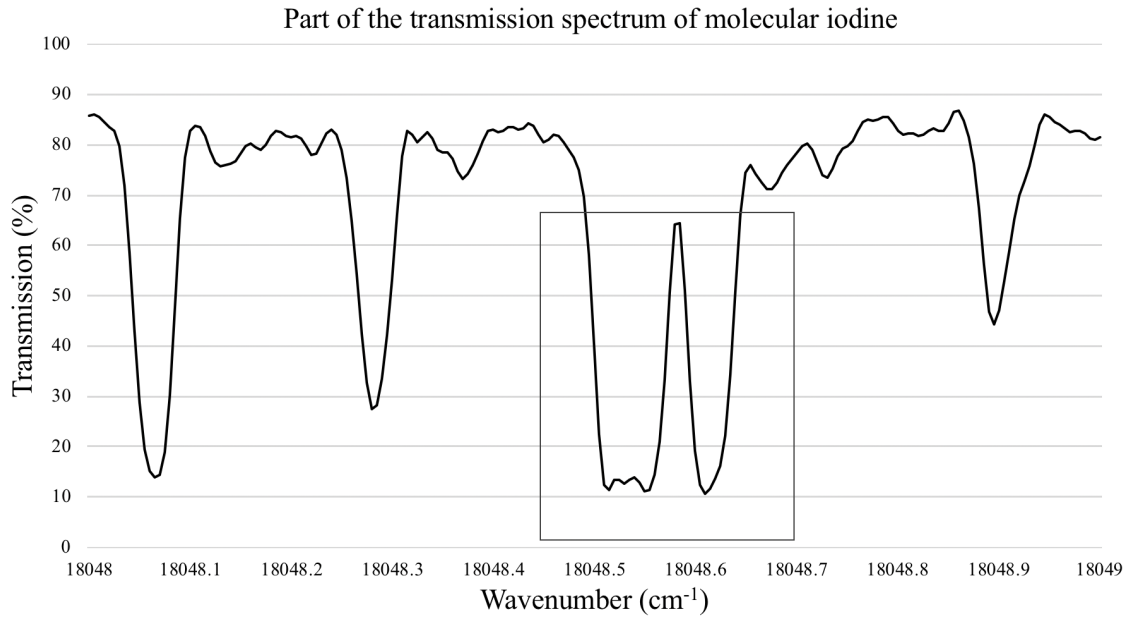


Figure 38: Region of the Doppler-broadened spectrum for iodine examined while performing current-driven frequency sweeps to obtain evidence of fluorescence at various locations. The box shows an area of initial recording of relatively-intense fluorescence. The black trace is the Doppler-broadened spectrum recorded by Salami and Ross [14].

It was chosen to stabilize the position of the gain-module grating and lock the laser to the PDH component of the system while sweeping frequency on a second servo controller connected to the iodine system.

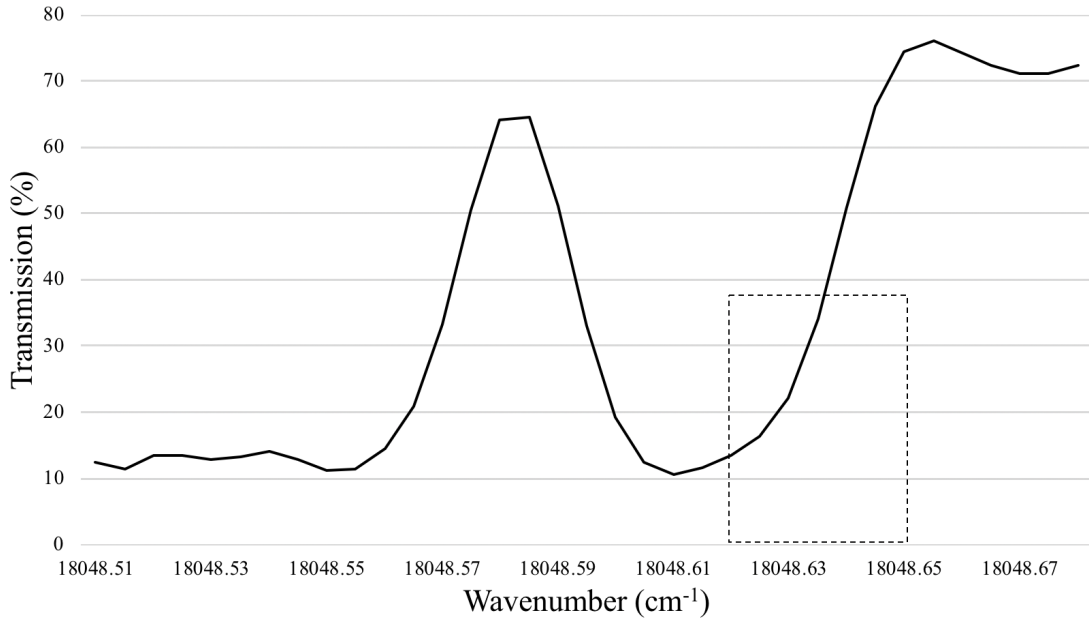


Figure 39: A magnification of the previously-boxed localized region of initial recording of fluorescence on the Doppler-broadened spectrum for iodine. The black trace is the Doppler-broadened spectrum recorded by Salami and Ross [14].

2.3.2 Observing Saturated Absorption

The entire system was designed to be compact and low-cost, and with these considerations propagating through the development of the project, the power of the laser was limited to that of the gain module output and efficiency of fiber-coupled components. This would serve to be one of the hurdles to overcome, but forced creativity in the optics, beam path, and electronics; which led to achieving results even while operating well below the presumed minimal threshold for laser power shown to be required in similar setups [19]. Using the location of the intense fluorescence and resonance as an initial location to seek out saturated absorption peaks, none were recognized during the first attempts. One possible reason was presumed to be a lack of enough overall beam intensity (< 2 mW incident on the system), so the PDH component of the system and the fiber beam splitter were removed in order to direct all of the power coming out of the SHG into the iodine system (~ 4 mW). Once

again, saturated absorption peaks were not visibly recognizable on the oscilloscope. The next aspect of the system to address was the overall alignment and beam diameters of both the pump and probe beams entering the iodine reference cell. Using additional lenses and a symmetrical placement on both sides of the reference cell, the pump and probe beams were approximately-collimated to both have a beam diameter of $< 400 \mu\text{m}$. The semi-transparent card technique previously mentioned was also utilized after beam waist reduction to ensure adequate beam overlap within the vapor cell. These adjustments and the removal of an unnecessary polarizing beam splitter are shown in Figure 40.

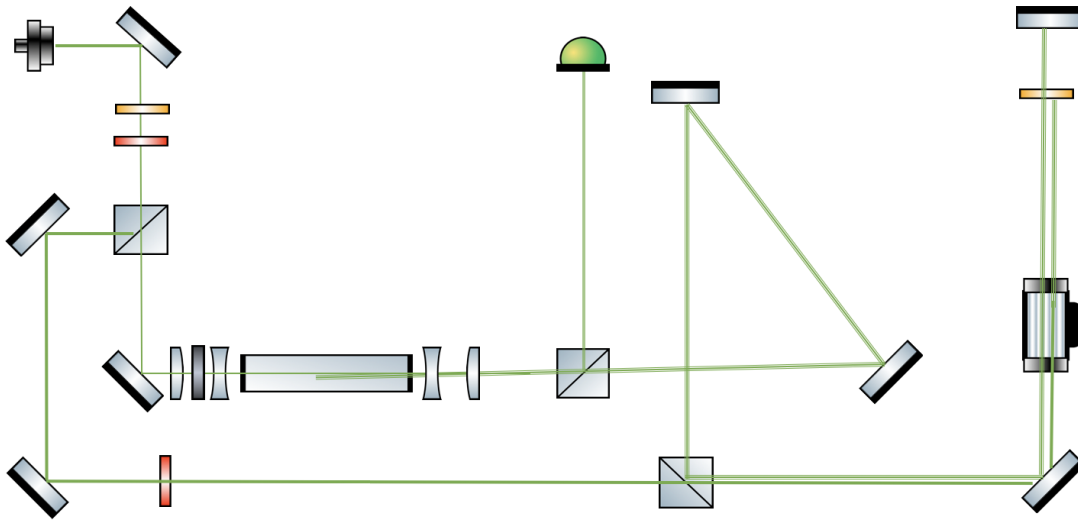


Figure 40: Diagram for the revised optical setup for the iodine lock. Key changes made included the removal of a polarizing beam splitter at the very beginning of beam propagation and the addition of lenses to drastically reduce the beam waist while increasing beam overlap within the iodine vapor cell.

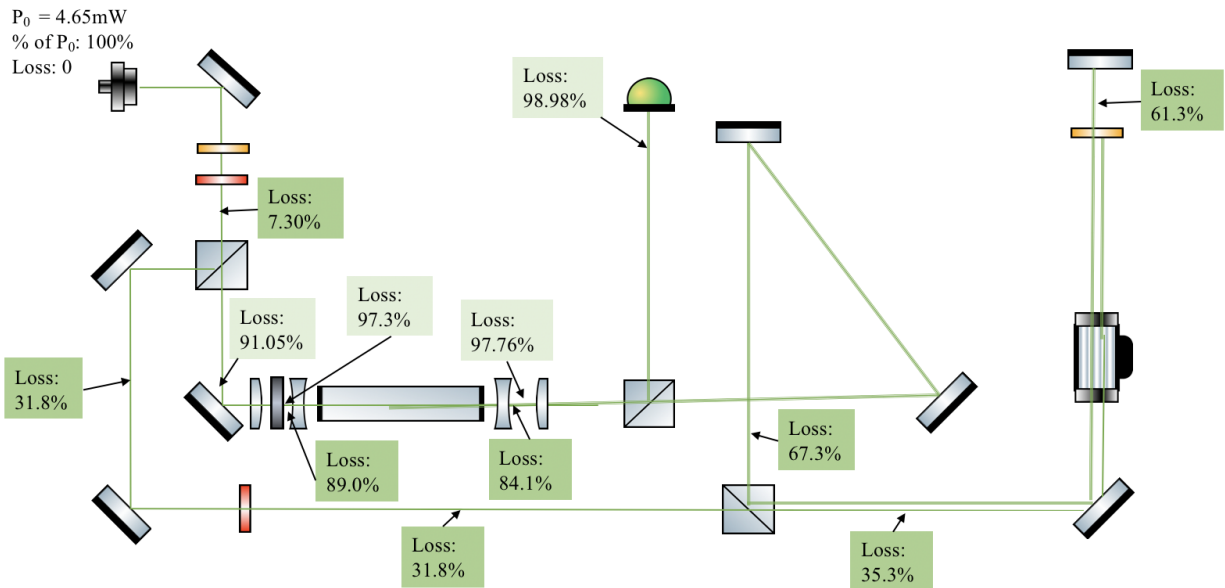


Figure 41: Power outputs and losses were measured at key sections within the optical setup to gain a better understanding of the system’s efficiency and overall design. P_0 is the power of the 554 nm beam incident on the system, where each labeled loss represents a power loss with respect to the incident power.

Careful alignment procedures were carried out at multiple points in the beam paths to ensure the pump and probe beams overlapped at each cross section within the reference cell. After seeking visual evidence of saturated absorption in the region of resonance previously focused on, small bumps were observed and measured to be spaced by ~ 60 MHz. The early visual evidence for saturated absorption is presented in Figure 42.

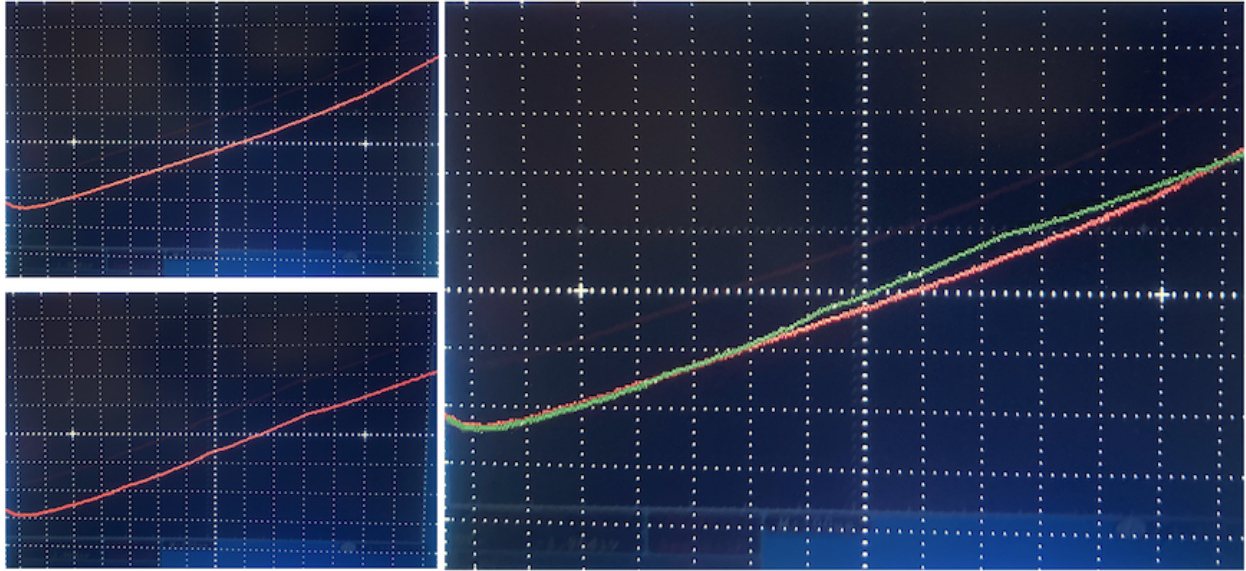


Figure 42: Top left: Only probe beam entering the vapor cell. Bottom left: Both probe and pump beam overlapping within the vapor cell. Right: Overlap of both graphics from the left, with evidence for saturated absorption represented as the green line. For this specific transition, each bump within the cluster was determined to be spaced by ~ 60 MHz. Here, the oscilloscope has a voltage division of 2.00 mV.

Although the observations served as visual evidence for saturated absorption occurring at this region, it was unclear if such a weak signal could yield an adequate error signal. Figure 43 shows fluorescence with "tighter" or reduced overlapping beam diameters within the vapor cell, which seemed to be a requirement for obtaining the observable saturated absorption with such a low-power pump-probe scheme.

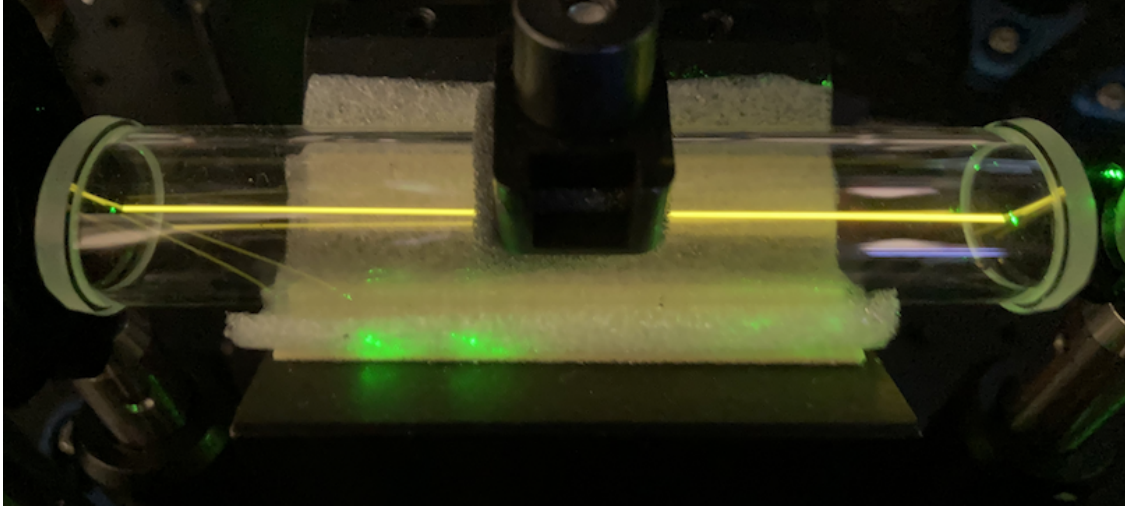


Figure 43: Fluorescence occurring within the iodine reference cell, as presented prior, however with a beam diameter of $< 400 \mu\text{m}$.

2.3.3 Locking to an Error Signal

The overall setup to obtain the error signals and lock the laser to an iodine transition was very similar to the setup described in the previous section presenting the PDH lock, with a few subtleties presented in Figure 44. Initially, observing an error signal was extremely difficult due to the low output signal coming from the iodine system's photodetector as a result of the low-power beam. This led to an amplification of the signal using a small coaxial amplifier (Mini-Circuits ZHL-6A+) driven by 18.0 V, which provided enough of a signal increase to yield adequate error signals as displayed in Figure 45. As a result, the laser was locked to an iodine transition found at $541.159480 \text{ THz} \pm 5 \text{ MHz}$ or approximately 553.98172 nm .

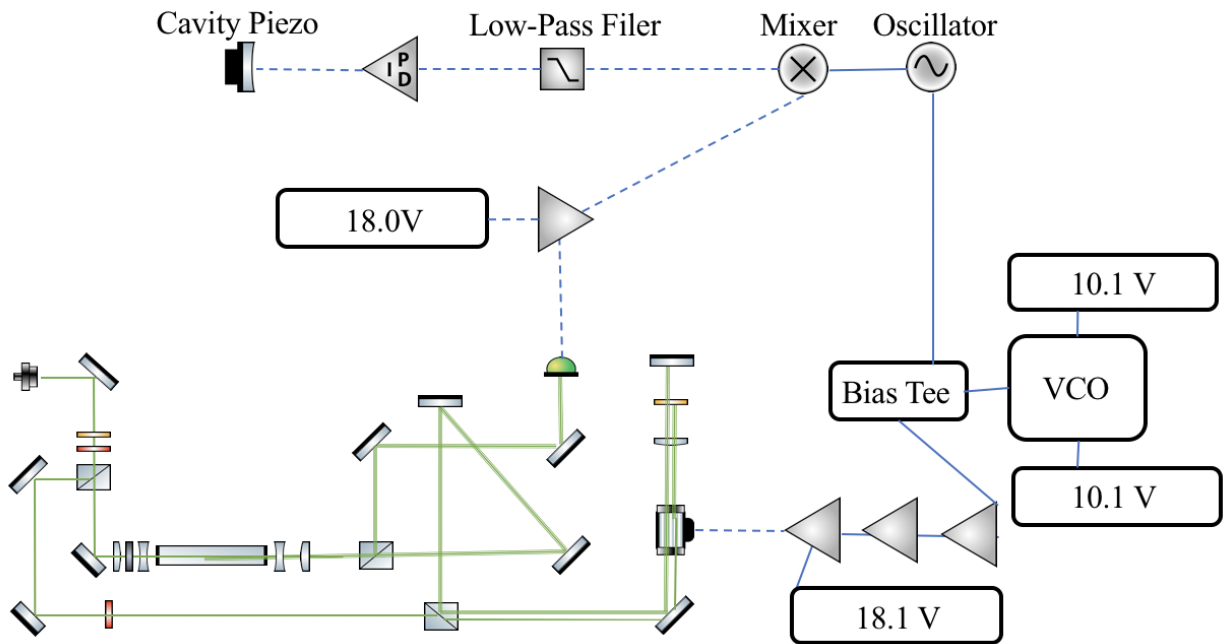


Figure 44: Electronics setup for the iodine lock. Here driving the AOM for frequency modulation is a VCO and dithering oscillator routed through a bias tee into multiple signal amplifiers to adequately drive the modulator. The same oscillator is mixed with an amplified photodetector signal and sent through a low-pass filter of 16 kHz and servo controller feeding back into the Fabry-Perot cavity piezo in this case. Initially during locking to an iodine transition, the PDH lock was bypassed and the iodine lock servo controller feedback was sent directly to the laser diode controller.

Unlike a simple pump-probe scheme presented in the application of saturation absorption spectroscopy, where each beam has the same frequency, the setup for this experiment incorporates the previously-mentioned AOM. As discussed, this provides a frequency modulation on the pump beam that allows for the generation of an error signal. Because of the modulation, the locking point for each respective hyperfine structure is actually shifted from the source laser's measured frequency ν_0 . With the double-pass AOM technique on the pump beam, the modulation of 160.1 MHz is doubled to 320.2 MHz ($+\delta\nu$) before interacting with the probe beam and iodine vapor. As the modulation is transferred to the probe beam, where phase conjugation occurs, the pump beam's modulation of $+\delta\nu$ is received at the photodetector with the probe beam as -320.2 MHz ($-\delta\nu$). The zero-crossing locking point for the error signal is then symmetrically in between ν_0 and $\nu_0 - \delta\nu$; therefore, the actual

frequency being locked to for each respective locking point is $\nu_0 - \frac{\delta\nu}{2}$.

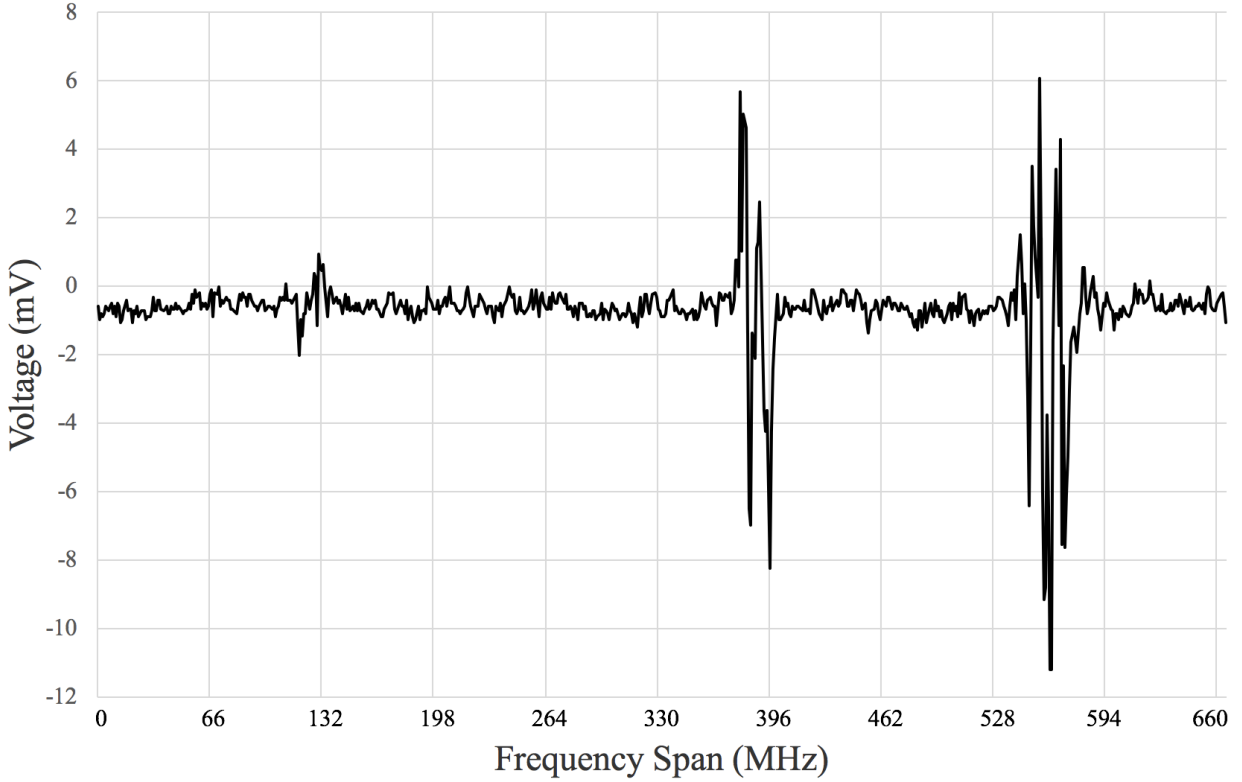


Figure 45: Error signals with a near-zero background using modulation transfer spectroscopy, representing locations of hyperfine structures for iodine during frequency sweeping with the servo controller. This is a snapshot showing closely-spaced clusters, characteristic of error signals of hyperfine structures.

Due to the modulation on a single beam, the velocity class of atoms or molecules jointly interacting with both counter-propagating beams is no longer when the atoms or molecules are stationary at ν_0 . Using the relationship between angular frequency of radiation ω in the laboratory frame of reference and the angular frequency observed in a moving frame with some velocity v , we can formulate an equality for two counter-propagating beams [26]; with one being modulated, as

$$\omega_0 + kv = \omega_0 - kv + \delta\omega, \quad (45)$$

where ω_0 represents the unmodulated beam frequency and k is the wavevector of the radiation with magnitude $k = \frac{\omega_0}{c} = \frac{2\pi}{\lambda}$. For this setup, it is assumed that $\vec{k} \cdot \vec{v} = kv$. Solving for

the velocity, we arrive at an equation for the velocity class of the iodine molecules in the experiment,

$$v = \frac{\delta\omega}{2k} = c \frac{\delta\omega}{2\omega_0}. \quad (46)$$

When plugging this result back into Equation 45 and applying a sign change due to the nature of modulation transfer, the frequency shift can be checked by

$$\omega_0 - \frac{\delta\omega}{2} = \omega_0 + \frac{\delta\omega}{2} - \delta\omega, \quad (47)$$

showing the location of the zero-crossing, where $\omega = 2\pi\nu$.

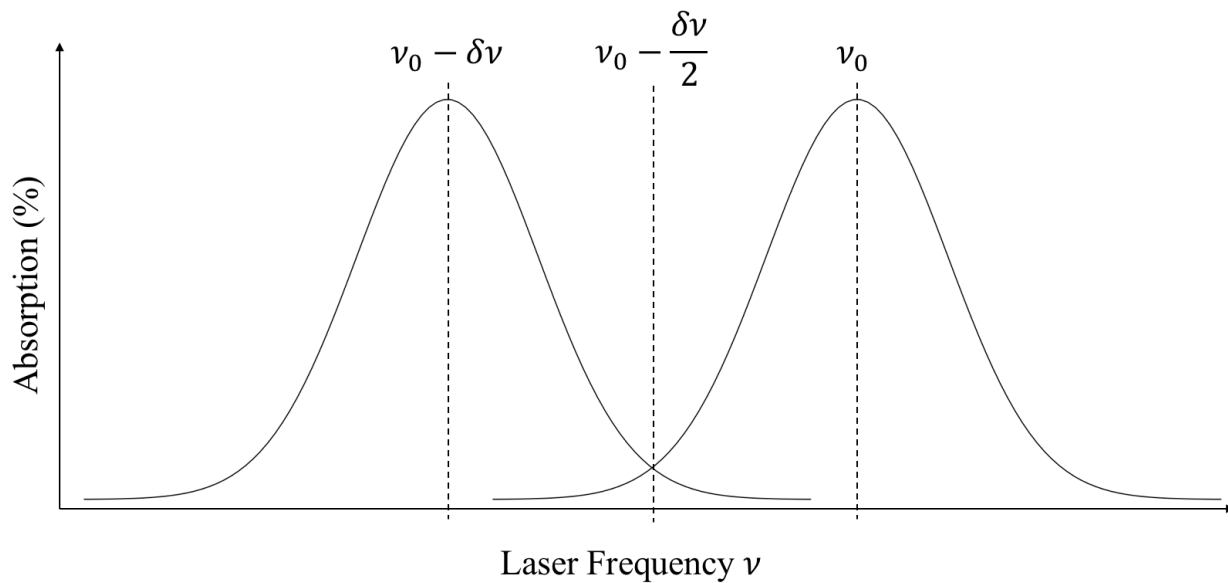


Figure 46: A visual representation of the presence of both a beam at some carrier frequency ν_0 and one with a modulation of $-\delta\nu$, with the zero-crossing at $\nu_0 - \frac{\delta\nu}{2}$.

3 Experimental Results

3.0.1 Experimental Iodine Spectrum

Initial frequency sweeps over a range of ± 700 MHz took place to support the accuracy of the region of the iodine spectrum being observed and were compared with the known transmission spectrum within the *Journal of Molecular Spectroscopy* [14]. Figure 47 shows a sample region where the Doppler-broadened spectrum was viewed using frequency sweeps in each focused area to observe transmission at each respective location.

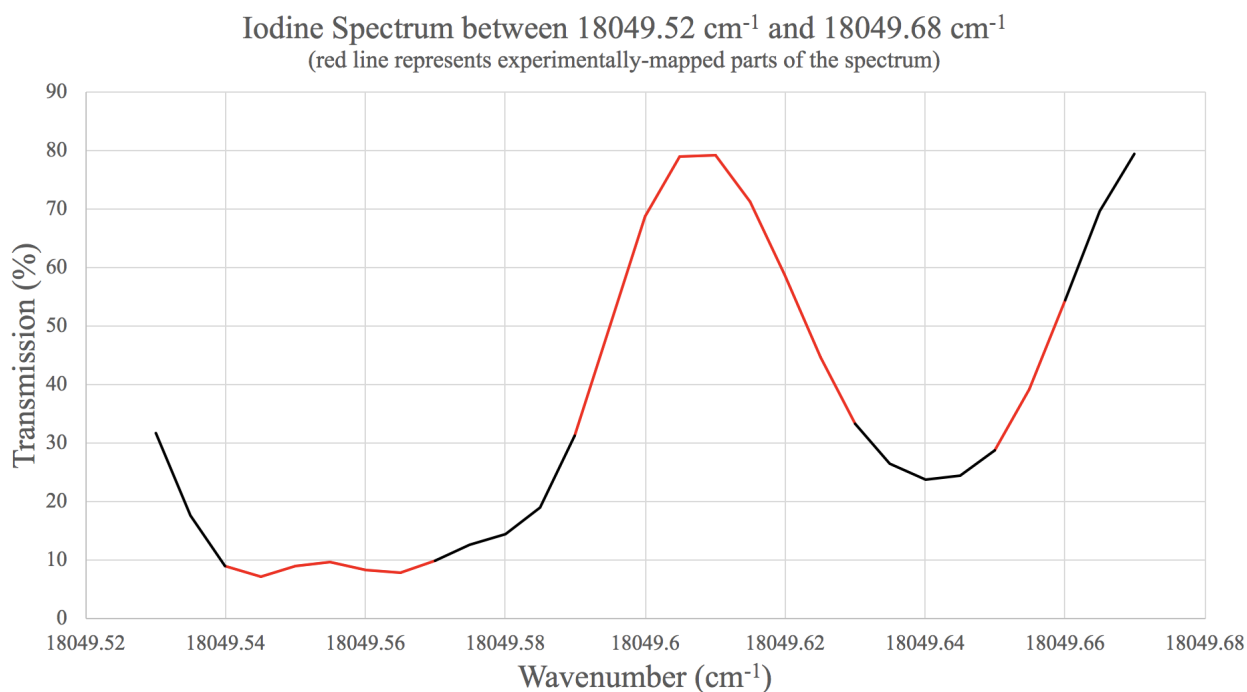


Figure 47: Confirmation of an examined region of the Doppler-broadened spectrum of iodine, where red regions of the spectrum represent those specifically mapped within an accuracy of ± 10 MHz. The black trace is the Doppler-broadened spectrum recorded by Salami and Ross [14].

The initial data obtained to map the spectrum and observe error signals representing hyperfine structures was found while the incident beam on the iodine system was tuned to ~ 541.11 THz, which showed to be a region of repeatedly lockable and stable error signals. Once

the system and electronics were determined to be reliable for locking, the gain module was manually tuned to a frequency of 540.859237 THz, which potentially would be ideal for subsequent phases of the encompassing project: a region on resonance with an ytterbium ion transition (^{171}Yb) using a third-harmonic generator [18].

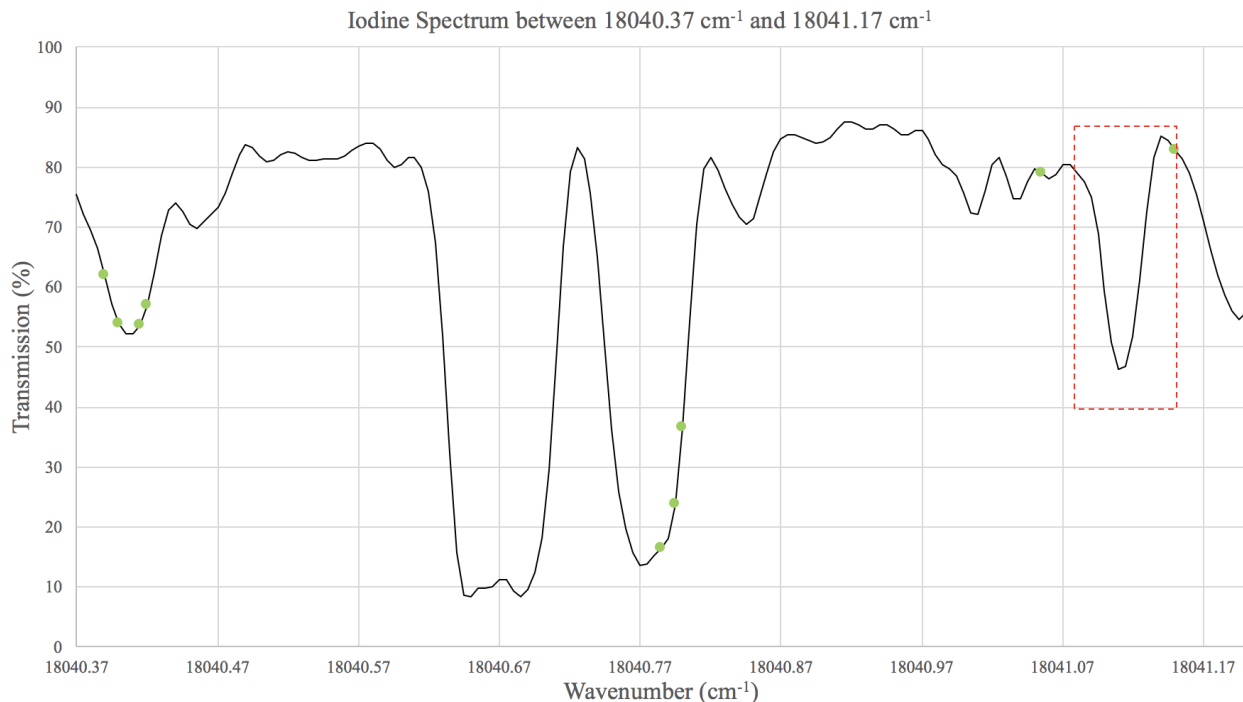


Figure 48: A region of the iodine spectrum (transmission (%) vs wavenumber (cm^{-1})) examined during initial frequency sweeps and locking to a respective iodine transition. Green dots represent initial findings for lockable error signals representing locations of hyperfine components. The red dotted box represents the mentioned region of interest. The black trace is the Doppler-broadened spectrum recorded by Salami and Ross [14].

Course tuning the laser system to a previously experimentally obtained frequency of 540.859237 THz was carried out through manual tuning of the feedback grating for the gain module. Once tuned to within hundreds of MHz, adjustments in diode controller current to 540 mA and gain module TEC temperature of 27.822 $^{\circ}\text{C}$ were performed in conjunction with an SHG TEC temperature of 47.561 $^{\circ}\text{C}$, ultimately to optimize power output at the desired frequency. With the PDH lock active, the power output entering the iodine system was at \sim

2.46 mW while sweeping ± 700 MHz around the frequency of 540.859237 THz and lockable error signals were found at numerous locations on the spectrum, provided in Table 2 and Figure 49.

Hyperfine Components	Measured Frequency (THz)	Absolute Frequency (THz)
a_1	540.858602	540.858442
a_2	540.858818	540.858658
a_3	540.858924	540.858764
a_4	540.859242	540.859082
a_5	540.859448	540.859288
a_6	540.859580	540.859420
a_7	540.859706	540.859546
a_8	540.859838	540.859678
a_9	540.859936	540.859776

Table 2: Frequency measurements of the molecular iodine R(146) 25-0 $a_1 - a_9$ hyperfine components found at 554 nm, where R(146) represents the rotational branch (P,R) and J assignment and 25-0 is the vibrational assignment [27]. Measured Frequency values were recorded on the wave meter and Absolute Frequency values take into account the AOM modulated-frequency shift. Error on the frequency values is ± 2 MHz due to the absolute accuracy of the wave meter [20].

As each error signal was found, absolute frequency was monitored with a wave meter (HighFinesse/Angstrom WSU-2), which has a manufacturer and lab-tested absolute frequency accuracy of within ± 2 MHz and a measurement resolution of 500 kHz. The hardware supports a standard calibration range between 600 nm and 800 nm [20], where this unit was calibrated using a 780 nm beam locked to a crossover resonance near the $5^2S_{1/2} \leftrightarrow 5^2P_{3/2}$ F=2 to F=3 transition for ^{87}Rb and at the calibrated frequency of 384.228115 THz [22]. The source of the monitored frequency was the split IR output on the gain module, therefore all frequency measurements herein include a doubling of frequency to adjust for second harmonic generation.

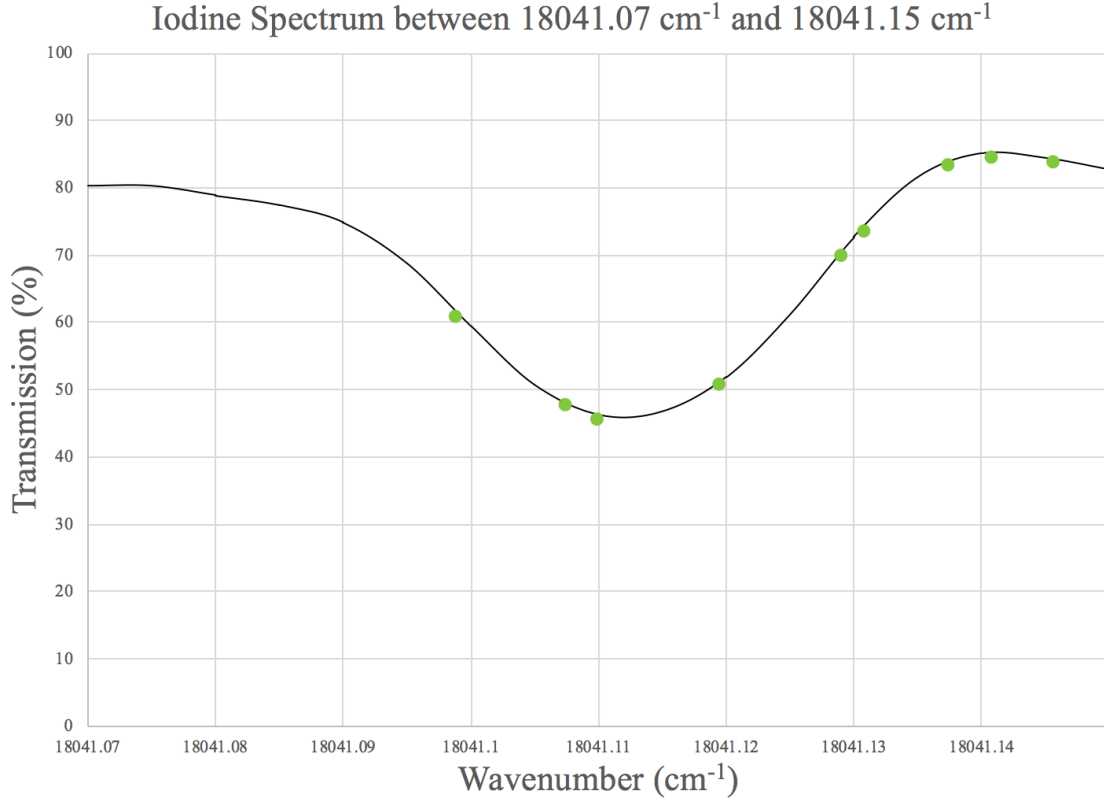


Figure 49: Error signal locations for hyperfine structures near 540.859237 THz. The black trace is the Doppler-broadened spectrum recorded by Salami and Ross [14].

3.0.2 Frequency Stability

All of the locations presented provided error signals that were easily lockable, with low-power (~ 3 mW) frequency stabilization (< 2 MHz) lasting up to ~ 40 minutes conjointly with the PDH locking component of the system, before slowly drifting in frequency (> 5 MHz). Both the PDH lock and iodine lock components of the laser stabilization system were used conjointly so that two servo controllers were simultaneously locked to the TEM₀₀ mode of the Fabry-Perot cavity and to an iodine transition using modulation transfer spectroscopy, respectively. Individual systems have been described in previous sections, however the feedback to the controllers were unique in setup.

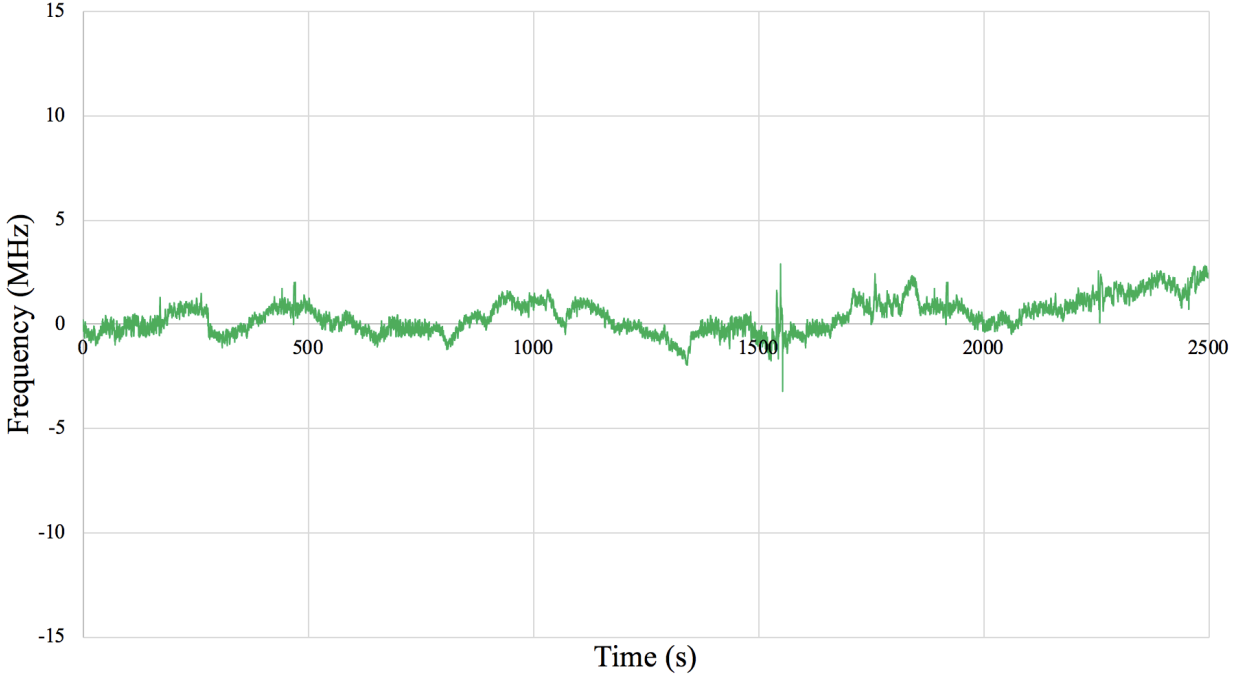


Figure 50: Initial frequency stability while locked to an error signal at 540.859082 THz for ~ 40 minutes. The large fluctuation around 1500 seconds was due to ambient noise.

The PDH lock was left alone so that the setup was identical to one without any attempts to further lock frequency to an iodine transition. The frequency was swept using driving-current and feedback was provided to the gain module diode controller. An adequate error signal was generated and locked to the respective servo controller. The locking electronics for the iodine transition were set up nearly exactly as they were without using the PDH component of the system, however frequency sweeps would be smaller (± 200 MHz) due to feedback being sent to the piezo controller via changes in voltage; therefore, yielding subtle variations to the Fabry-Perot cavity length to finely tune frequency for the respective iodine transition. Signal flow for the jointly-locking system was as follows: gain module output fed into a spliced isolator and a 99:1 fiber splitter with 1% for frequency monitoring and 99% into the SHG, where output was split using a 75:25 fiber splitter. The 25% output was coupled into the fiber EOM that was fiber-coupled into the fiber port for the PDH lock, and the 75% output was coupled directly to another fiber port for the iodine lock. It was determined

that a minimum of ~ 2.12 mW of an incident beam was needed directly into the iodine lock system in order to observe adequate error signals for locking stability.

While beam inputs and observation of error signals for both the PDH component and iodine component of the entire system were substantial for jointly-locking for frequency stabilization, consistently locking both did take some finesse. It became apparent there would be a higher probability of successful joint-locking when relatively strong error signals were observed for both components of the system while slowly alternating between each respective servo controller as sweep attenuation was adjusted for locking. Once the sweeps were both attenuated and the low frequency gain limit (LFGL) switch was engaged (P-I filter is enabled with a low frequency gain limit) on each LB1005 controller for stable error signals, the PDH servo switch was flipped "on" (P-I filter is enabled with full integrator and low frequency gain limit is disabled) while additional piezo sweeps were executed to similarly lock the iodine servo to an error signal.

It should be noted that additional data collection of iodine transitions and frequency stabilization was postponed due to a gain module failure which compromised the mode of the 1108 nm source, ultimately yielding poor beam quality and a greatly-reduced power output throughout the entire system. This led to re-splicing fiber components into new gain module units, however due to continued output and potential polarization issues the new modules are still undergoing further testing to solve these problems and build upon the research herein.

4 Looking Ahead

4.1 Hardware

Many of the system parts for the project were pulled from previously-existing projects that were no longer in use and subsequent components were then constructed upon them. While

this accomplished the early goals of using methods and devices with known performances and keeping costs low, it proved to immensely hinder system optimization down the road.

The gain module aluminum platform was one of the previously used components, which worked for the project, however there are better setups which would have made the project run more efficiently with an increase in overall performance. Instead of using the gain module platform with screw holes and custom soldered connectors, it seems better in hindsight to simply incorporate a 14-pin butterfly laser diode mount. A butterfly unit would have provided greater stability of the gain module and pin connections, which would have potentially led to only having to use a single gain module instead of there being failures which may have been the result of faulty connections; although feedback from the manufacturer is in the process of being provided. The butterfly mount would have also provided all necessary connections. With the setup presented herein, all gain module and controller connections were completely custom soldered; which greatly increased the susceptibility of failures. The gain module platform was also not conducive to incorporating an additional kinetic mount for the aspheric collimating lens in between the module and the grating. For this system, the aspheric lens was epoxied to a kinetic lens mount and screwed into the platform using an additional securing plate. This was a great improvement to a very early attempt to epoxy the lens directly to the platform using a small plastic mount, however the kinetic mount restricted placement of the grating mount merely due to the bulkiness of each component. After the construction of the system and experimentation with it, I believe these few changes to the mounting hardware would have made an enormous impact on the entire system and its performance.

Due to the laboratory door opening and closing during data collection, the through-holes (implemented for a vacuum environment) on the Fabry-Perot cavity led to abrupt changes of the index of refraction within the cavity and the "spikes" discussed when presenting

frequency stabilization data. Since the cause of each fluctuation in the frequency plots is known to be this, the data presented served its purpose of demonstrating stability. However for future monitoring and data collection, the through-holes will be plugged to avoid the issue.

The gain module was the workhorse for the system constructed herein and served its purpose, however due to the combined power requirements of each component of the system(s) moving forward (PDH lock, SHG for the iodine lock, and THG for future ion experiments), a more powerful and robust laser system with amplification is being considered to provide ~ 1.5 W of 1108 nm incident on the system; a substantial increase from a ~ 200 mW. This will allow for adequate power to be on the frequency stabilization components of the entire system while granting multiple beam pick-offs with an abundance of power for frequency tripling and experimentation using a 369 nm beam.

4.2 Moving Forward

The project has yielded substantial evidence for the ability to adequately lock to an iodine reference using modulation of an 1108 nm source. Furthermore, my work herein provides a guideline for accomplishing this task with a low-cost commercial off-the-shelf gain module unit, various relatively-inexpensive components readily available, and some custom work that can be very educational; while providing a strong foundation for developing a low-power means to adequately stabilize laser frequency to < 2 MHz and make precision measurements of hyperfine components within ± 2 MHz. Due to the nature of the system design and methods presented herein, the project can serve incoming lab personnel and students with an amazing opportunity to learn as they build something of great value in any AMO lab. This project and some of its components will certainly evolve for efficiency and increased stabilization of laser frequency as it becomes deeply integrated within the progress of future experiments.

Statement of Independent Work

I declare that this thesis was composed solely by myself, that the work contained herein is my own except where cited, and that this body of work has not been submitted for any other degree or qualification.

5 Bibliography

References

- [1] Black, E. D. "An introduction to Pound Drever Hall laser frequency stabilization," American Journal of Physics 69, 79-87 (2001).
- [2] Menzel, R. (2007). Photonics: linear and nonlinear interactions of laser light and matter. Springer.
- [3] Acousto-optic modulator s/n 456216: Instruction manual. (2021). IntraAction Corp.
- [4] Fiber coupled curved stripe gain chip for 1000-1150nm tuning range. (2021). Innolume GmbH.
- [5] Supplee, J. M., Whittaker, E. A., and Lenth, W. "Theoretical description of frequency modulation and wavelength modulation spectroscopy," Applied Optics 33, 6294-6302 (1994).
- [6] Hui, R. (2020). Passive optical components. Introduction to fiber-optic communications. (pp. 209-297) Academic Press.
- [7] Hui, R. (2020). Photodetectors. Introduction to fiber-optic communications. (pp. 125-154) Academic Press.
- [8] LB1005 High-speed servo controller: Operating manual. (2020). New Focus.

- [9] Hui, R., O'Sullivan, M. (2009). Fiber optic measurement techniques (pp. 116-121). Elsevier.
- [10] Vapor Reference Cells: Overview. (2021). Thorlabs.
- [11] Bjorklund, G. C. "Frequency-modulation spectroscopy: a new method for measuring weak absorptions and dispersions," *Opt. Lett.* 5, 15-17 (1980).
- [12] Barry, J. F., (2013). Laser cooling and slowing of a diatomic molecule [Dissertation in candidacy for the degree of doctor of philosophy]. Yale University.
- [13] Shin, D.K., Henson, B.M., Khakimov, R.I., Ross, J.A., Dedman, C.J., Hodgman, S.S., Baldwin, K.G.H., and Truscott, A.G. "Widely tunable, narrow linewidth external-cavity gain chip laser for spectroscopy between 1.0 and 1.1 μm ," *Opt. Express* 24, 27403-27414 (2016).
- [14] Salami, H., Ross, A.J. "A molecular iodine atlas in ascii format" *Journal of Molecular Spectroscopy*, Vol 233, Issue 1, 157-159 (2005).
- [15] Valeur and M. N. Berberan-Santos, *Molecular Fluorescence: Principles and Applications*, 2nd Ed. Wiley-VCH (2012).
- [16] H. Kogelnik and T. Li, "Laser beams and resonators," in *Proceedings of the IEEE*, vol. 54, no. 10, pp. 1312-1329, Oct. 1966.
- [17] Leith, E.N. (2005). *Encyclopedia of modern optics: phase conjugation and image correction*. (pp. 87-93) Elsevier.
- [18] Olmschenk, S.M. (2009). Quantum teleportation between distant matter qubits (Order No. 3382319) [Doctoral dissertation, University of Michigan]. ProQuest Dissertations & Theses Global. (304929456).

- [19] Hsiao, Y., Kao, C., Chen, H., Chen, S., Peng, J., and Wang, L., "Absolute frequency measurement of the molecular iodine hyperfine transitions at 548nm," J. Opt. Soc. Am. B 30, 328-332 (2013).
- [20] Angstrom WS Ultimate 2: User manual. HighFinesse/Angstrom.
- [21] Rost, F.W.D. (1992). Fluorescence Microscopy. Cambridge University Press. p. 22.
- [22] Daniel A. Steck, "Rubidium 87 D Line Data" available online at <http://steck.us/alkalidata> (revision 2.2.2, 9 July 2021).
- [23] Thomas, G., Stamnes, K. (2017). Radiative Transfer in the Atmosphere and Ocean. 2nd Ed. Cambridge University Press (1999).
- [24] Preston, D.W. (1996). "Doppler-free saturated absorption: Laser spectroscopy" American Journal of Physics. 64 (11): 1432-1436.
- [25] Demtroder, W. (2013). "Laser spectroscopy: Basic concepts and instrumentation" Springer Science & Business Media.
- [26] Foot, C.J. Atomic Physics New York, NY. Oxford University Press (2005).
- [27] Simmons, J. D., & Hougen, J. T. (1977). Atlas of the I₂ Spectrum from 19 000 to 18 000 cm⁻¹. Journal of Research of the National Bureau of Standards. Section A, Physics and Chemistry, 81A(1), 25-80.
- [28] Li, L. Z., Park, S. E., Noh, H. R., Park, J. D., and Cho, C. H. "Modulation transfer spectroscopy for a two-level atomic system with a non-cycling transition," J. Phys. Soc. Jpn. 80, 074301 (2011).
- [29] Shirley, J. H. "Modulation transfer processes in optical heterodyne saturation spectroscopy," Opt. Lett. 7, 537-539 (1982).